



PONTIFICIA UNIVERSIDAD CATÓLICA DE CHILE  
ESCUELA DE INGENIERÍA

# **ENERGY-TRANSFORM FORMULATION FOR SOFT-TISSUE MECHANICS SIMULATIONS**

**PATRICIO ZAVALA FUENZALIDA**

Thesis submitted to the Office of Research and Graduate Studies  
in partial fulfillment of the requirements for the degree of  
Master of Science in Engineering

Advisor:  
DANIEL HURTADO

Santiago de Chile, October 2020

© MMXX, PATRICIO ZAVALA FUENZALIDA



PONTIFICIA UNIVERSIDAD CATÓLICA DE CHILE  
ESCUELA DE INGENIERÍA

# ENERGY-TRANSFORM FORMULATION FOR SOFT-TISSUE MECHANICS SIMULATIONS

**PATRICIO ZAVALA FUENZALIDA**

Members of the Committee:

DANIEL HURTADO

FRANCISCO SAHLI COSTABAL

CLAUDIO GARCIA HERRERA

FRANCO PEDRESCHI PLASENCIA

D.H.H.  
F.C. Sahli  
  


Thesis submitted to the Office of Research and Graduate Studies  
in partial fulfillment of the requirements for the degree of  
Master of Science in Engineering

Santiago de Chile, October 2020

© MMXX, PATRICIO ZAVALA FUENZALIDA

*To my family and beloveds, for  
always being there for me.*

## ACKNOWLEDGEMENTS

I wish to thank to my advisor, Daniel Hurtado, for his guidance, advice, and support from the first course in which he was my teacher, Continuum Mechanics. His constant motivation and challenges showed me a new and exciting path for my life. It has been a pleasure to learn from him, and I hope to collaborate with him in future projects. I also wish to thank the commission members, Franco Pedreschi, Claudio García Herrera and Francisco Sahli, for their time and constructive feedback.

During the two and a half years of my master's studies, I had the support and advice of my partners at the laboratory Mauricio Sarabia, Carlos Andrade, William Ramírez, David Ortiz, Felipe Álvarez, Agustín Pérez, Pablo Bascuñan, Agustín Cox, Francisco Sahli, Felipe Concha, Rodrigo Quezada, and Roberto León. I want to thank them for that and for the pleasant place to work they gave me.

I also want to thank my team in the Engineering Selection and all the beautiful people I knew, thanks for all the experiences and personal growth. Further, I want to especially thank the IEDIEG Student Chapter and Proyecto UC to motivate me to make social volunteer projects during my eight years at Pontificia Universidad Católica de Chile. I thank each of them for never letting me fall or quit and for all these years and moments that I will never forget.

Finally, I want to thank my girlfriend, Jennifer Galleguillos, and my family, for their support during all these years. To my brothers Carlos, and Santiago, and my sister, Danae, for their understanding, company, and advice and accompaniment. Special thanks to my

parents, Patricio Zavala and Danae Fuenzalida, because no matter which path I took or what problem I faced, they never left me alone, and they gave me the love and support I needed.

## TABLE OF CONTENTS

ACKNOWLEDGEMENTS	iv
LIST OF FIGURES	viii
LIST OF TABLES	x
ABSTRACT	xi
RESUMEN	xii
1. INTRODUCTION	1
1.1. Motivation . . . . .	1
1.2. Heart anatomy, structure and function . . . . .	2
1.3. Vessel anatomy, structure and function . . . . .	4
1.4. Notions of Continuum Mechanics . . . . .	6
1.5. Cardiac tissue constitutive modeling . . . . .	9
1.6. Artery tissue constitutive modeling . . . . .	10
2. ACCELERATING CARDIAC AND VESSEL MECHANICS: AN ENERGY TRANSFORMED VARIATIONAL FORMULATION FOR HYPERELASTIC BIOSOLIDS	13
2.1. Introduction . . . . .	13
2.2. Energy-transformed variational formulation of the hyperelastic problem and finite-element discretization . . . . .	16
2.2.1. Standard variational formulations for the quasi-incompressible and incompressible hyperelasticity problems . . . . .	16
2.2.2. Energy-transform variational formulations for the hyperelasticity problem	19
2.2.3. Linearization of the weak form . . . . .	32
2.2.4. Multi-field finite-element discretization and solution . . . . .	34
2.3. Numerical simulations . . . . .	35

2.3.1. Cardiac beam benchmark . . . . .	37
2.3.2. Artery inflation . . . . .	42
2.3.3. Passive filling of biventricular chambers . . . . .	47
2.4. Discussion . . . . .	51
3. CONCLUSION	56
4. FUTURE WORK	57
BIBLIOGRAPHY	59

## LIST OF FIGURES

1.1	Heart anatomy showing the four chambers and the blood flux. Taken from Guyton and Hall (2016). . . . .	3
1.2	Fibers incorporated into a biventricular model. . . . .	4
1.3	The major components of the cardiovascular system: circulating blood, the blood vessels, and the heart. Taken and modified from Iaizzo (2015) . . . . .	5
1.4	Artery anatomy showing the major components of a healthy artery. Taken from Holzapfel, Gasser, and Ogden (2000). . . . .	7
1.5	Schematic representation of the residual stresses. Figure shows a segment of an artery in the (stress-free), in the load-free configuration, and in the current configuration. Taken from Holzapfel et al. (2000). . . . .	11
2.1	Geometry and loading of three examples of cardiovascular simulations: (a) Cardiac beam benchmark (mesh with 208 nodes and 648 elements), (b) Artery inflation (mesh with 1,661 nodes and 4,896 elements), (c) Biventricular chambers under passive filling (mesh with 8,612 nodes and 37,127 elements). . . . .	36
2.2	Constitutive models and parameter values for the simulations considered in this study. . . . .	37
2.3	Cardiac beam benchmark. (a) Points along the beam axis where strain was reported, (b) Local axis for the beam cross-section. Based on Land et al. (2015). . . . .	38
2.4	Plot of strain along the line in directions of x-, y- and z-axes (quasi-incompressible approach) compared with results obtained by PUC-FEAP team Land et al. (2015). . . . .	39
2.5	Plot of strain along the line in directions of x-, y- and z-axes (full-incompressible approach) compared with results obtained by PUC-FEAP team (Land et al., 2015). . . . .	40

2.6	Condition number for the cardiac beam benchmark example under different formulations and element interpolation schemes: (a) Quasi-incompressible case (b) Fully-incompressible case . . . . .	42
2.7	Artery inflation simulation. (a) fiber stretch, (b) stress along the fiber direction . . . . . 44figure.2.8	43
2.9	Condition number for several discretizations and element combinations for artery inflation. (a) quasi-incompressible case. (b) full-incompressible case. . . . .	47
2.10	(a) : model with fibers included (b): square stretching in the direction of the fiber (c): stress in the direction of the fiber (d): Von Mises stress for the final state. . . . .	49

## LIST OF TABLES

2.1	Numerical performance of the ETVF and Standard FE models for the cardiac beam benchmark example in the quasi-incompressible case ( $\kappa = 10^3$ ). . . . .	41
2.2	Numerical performance of the ETVF and Standard FE models for the cardiac beam benchmark example in the fully-incompressible case. . . . .	41
2.3	Geometry and fiber orientation for the artery inflation example. . . . .	43
2.4	Numerical performance of the ETVF and Standard FE models for the artery inflation example in the quasi-incompressible case ( $\kappa = 10^3$ ). . . . .	45
2.5	Numerical performance of the ETVF and Standard FE models for the artery inflation example in the fully-incompressible case. . . . .	46
2.6	Numerical performance of the ETVF and Standard FE models for the biventricular passive inflation example in the quasi-incompressible case ( $\kappa = 10^4$ ). . . . .	50
2.7	Numerical performance of the ETVF and Standard FE models for the biventricular passive inflation example in the fully-incompressible case. . . . .	51

## ABSTRACT

Computational modeling constitutes a powerful tool for simulating the biomechanical function of human organs such as the heart and the aorta. However, the high dimensionality and the non-linear nature of these models translate into challenging computational demands in terms of wall-clock time. In this work, we present a novel energy-transform variational formulation (ETVF) for accelerating the numerical simulation of hyperelastic biosolids. To this end, we propose a mixed variational framework, where we introduce auxiliary fields that render the strain energy density into a quadratic form, at the expense of adding unknown fields to the problem. We further reduce the non-linearity of the problem by transforming the constraints that arise due to auxiliary fields in a Lagrange multiplier formulation. The resulting continuous problem is solved by using multi-field non-linear finite-element schemes. We assess the numerical performance of the ETVF by solving two benchmark problems in cardiac and vessel mechanics and one anatomically-detailed model of a human heart under passive filling that assumes an orthotropic heterogeneous constitutive relation. Our results show that the ETVF can deliver speed-ups up to  $2.28\times$  in realistic cardiovascular simulations only by considering the proposed reformulation of the hyperelastic problem. We further show that the decrease in computational cost is explained by the ability of the ETVF to reduce the condition number of tangent operators. We believe the ETVF offers an attractive framework to accelerate cardiovascular simulations that can be further combined with state-of-the-art techniques in parallel computing to solve large-scale problems in attractive computing times. Codes are available for download at <https://github.com/dehurtado/ETVF>.

**Keywords:** Mixed formulations, cardiac mechanics, artery simulations, condition number, non-linear finite element analysis

## RESUMEN

Los modelos computacionales constituyen una herramienta poderosa para simular la función biomecánica de órganos humanos, tales como el corazón o la aorta. Sin embargo, la alta dimensionalidad y la naturaleza no-lineal de estos modelos se traduce en grandes demandas computacionales en términos de tiempo de cómputo. En este trabajo, presentamos una nueva formulación variacional basada en la transformación de energía (ETVF) con el objetivo de acelerar las simulaciones numéricas de biosólidos hiperelásticos. Para este fin, proponemos un marco variacional mixto, donde introducimos campos auxiliares que transforman la función densidad de energía de deformación en una expresión cuadrática a expensas de añadir incógnitas al problema. Además, redujimos la no-linealidad del problema transformando las restricciones que aparecen debido a los campos auxiliares en una formulación de multiplicadores de Lagrange. El problema continuo resultante es resuelto mediante esquemas multicampo de elementos finitos no-lineales. Además, evaluamos el desempeño de las ETVF resolviendo dos problemas de referencia de mecánica cardíaca y arterial y uno de un modelo anatómicamente detallado de un corazón humano bajo llenado pasivo que posee una relación constitutiva heterogénea y ortotrópica. Nuestros resultados muestran que las ETVF pueden arrojar aceleraciones de hasta  $2.28\times$  en simulaciones cardíacas realistas, solo considerando la nueva formulación propuesta del problema de hiperelasticidad. Además, mostramos que la disminución del costo computacional es explicado por la habilidad de las ETVF para reducir el número de condicionamiento del operador tangente. Creemos que las ETVF ofrecen un marco atractivo para acelerar las simulaciones cardíacas, las que pueden ser además combinadas con técnicas de vanguardia en

computación en paralelo de alto rendimiento (HPC), para resolver problemas a gran escala en tiempos de cómputo atractivos. Los códigos están disponibles para descargar en <https://github.com/dehurtado/ETVF>.

**Keywords:** Formulaciones mixtas, mecánica cardíaca, simulaciones arteriales, número de condicionamiento, análisis de elementos finitos no-lineales.

# 1. INTRODUCTION

## 1.1. Motivation

Computational modeling and numerical simulations have increasingly gained attention since they constitute powerful tools for the medical community in the assessment of the functioning of human organs (Winslow, Trayanova, Geman, & Miller, 2012; Quarteroni, Lassila, Rossi, & Ruiz-Baier, 2017). In particular, current models for cardiac tissue and arterial walls are based on a continuum mechanics framework, and are benefited from hyperelasticity theory. Since these tissues must support large deformations displaying a non-linear constitutive response over complex geometries, numerical techniques as the finite element analysis are widely used by the community.

Although biomechanical simulations have successfully represented human organs function, there is an outstanding demand to reduce the computing time that these simulations require. Current models are constructed upon detailed and complex geometries that translate into systems with several millions of degrees of freedom that must be solved at each time step. High-performance parallel computing (HPC) is one alternative to solve the large system of equations that arise from the hyperelasticity problem (Lafortune, Arís, Vázquez, & Houzeaux, 2012). However, HPC increases budget costs to levels prohibitively high. Consequently, medically relevant experiments, many of them implemented using HPC, are critically dependent on available infrastructure and resources. This work aims to accelerate the solution of the hyperelastic problem by introducing a novel energy-transform variational formulation (ETVF) for soft-tissue mechanics.

This thesis is presented in four chapters. The first chapter is an introduction to the research and the theoretical framework in which it is based. The second chapter is the

article associated with this thesis entitled "Accelerating cardiac and vessel mechanics simulations: An energy-transform variational formulation for soft-tissue hyperelasticity." The third chapter presents the conclusions. Finally, the fourth chapter provides recommendations and ideas for future work.

## **1.2. Heart anatomy, structure and function**

The heart is the organ responsible for collecting blood from tissues and pump it to the lungs as well as receiving blood from the lungs and pump it to all tissues of the body. Its functioning is comparable to a pump, composed of four chambers, including two upper atria, with the primary function of collecting blood, and two lower chambers or ventricles, which are much more robust and function to pump blood out of the heart. The atrioventricular septum divides atria and ventricles into left and right. The purpose of the right atrium (RA) and the right ventricle (RV) is to receive blood from the body and drive it to the lungs. In contrast, the role of the left atrium (LA) and the left ventricle (LV) are to collect blood from the lungs and pump it to the rest of the body. Consequently, the internal pressure level into the left side of the heart is higher than on the right side, and the cardiac tissue (called myocardium) is much thicker in LV than in the RV. (Iaizzo, 2015; Göktepe, Acharya, Wong, & Kuhl, 2011).

At a cellular level, the heart is formed by millions of electrically excitable cardiac muscle cells, called cardiomyocytes, embedded in an extracellular matrix compounded by collagen. At the tissue level, the myocardium can contract actively and relax passively and involuntarily. Since the myocardium's passive behavior supports the internal pressures during the filling phase in diastole, the myocardium's active behavior is responsible for pumping the accumulated blood around the body. From an anatomical point of view, cardiomyocytes are arranged in muscular fibers, aligned with a macroscopic preferred direction, called fiber direction, which changes smoothly from endocardium to epicardium. In parallel, the extracellular matrix defines the sheet direction, while the

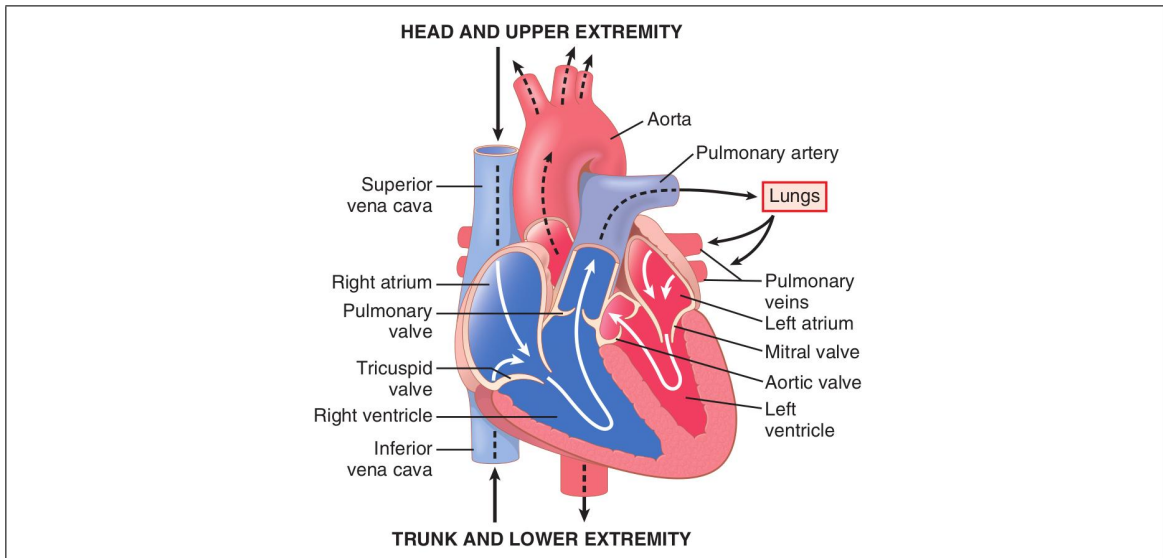


Figure 1.1. Heart anatomy showing the four chambers and the blood flux.  
Taken from Guyton and Hall (2016).

cross product of the other two represents the cross-sheet direction (Hurtado, Castro, & Gizzi, 2016; Bayer, Blake, Plank, & Trayanova, 2012). This complex physiology strongly influences the mechanical response of the cardiac tissue. In effect, studies carried out by Streeter *et al.*, and LeGrice *et al.* showed that the stiffness is higher in the fiber direction (Streeter & Sonnenblick, 1969; LeGrice *et al.*, 1995). Consequently, the models used in computational mechanics to simulate the heart function must consider the myocardium tissue as an highly anisotropic material (see figure 1.2). A normal heart operates following the cardiac cycle, which is divided into two phases: systole and diastole. Systole involves the contraction and ventricular ejection, while the diastole concerns to the rest of the process, including ventricular passive filling and relaxation (Iaizzo, 2015). The measurement and analysis of the pressure and volume changes in chambers during the cardiac cycle, especially in the left ventricle, deliver powerful insights to doctors to assess the heart function.

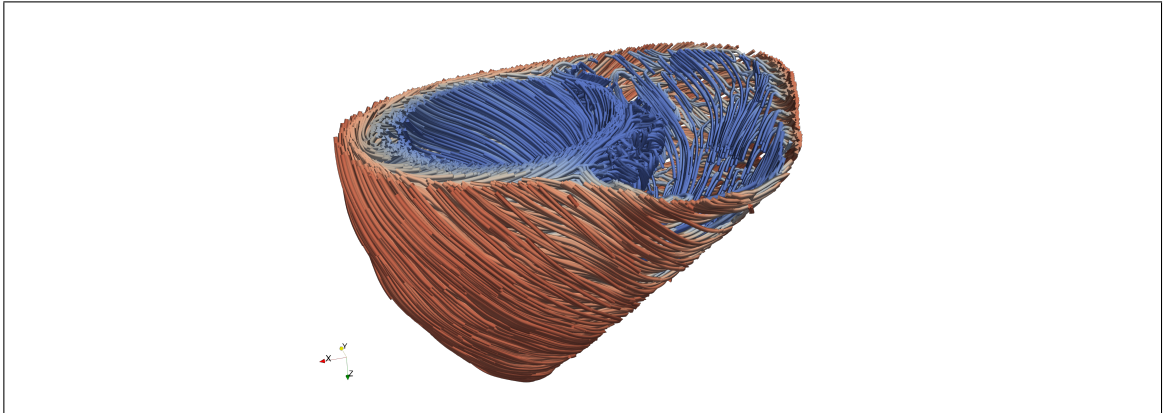


Figure 1.2. Fibers incorporated into a biventricular model.

Physicians can measure the changes in pressure and volume in chambers during the cardiac cycle, especially in the left ventricle, to get insights and indicators to assess heart function. One tool widely used in practice is called the pressure-volume loop diagram, from where doctors extract clinical indicators such as the ventricular volume in the end-diastole (EDV) and systole (ESV). At the same time, the stroke volume (SV) is a quantity that represents the blood volume pumped to the rest of the body and can be computed as the difference between EDV and ESV. Besides, the ejection fraction (EF) determines the percentage of the blood that the ventricle pumps each time it contracts and can be calculated as the ratio between SV and EDV. Alterations in SV and EDV values, along with changes in the pressure-volume loop shape, are a sign of pathology such as heart failure or valve diseases.

### **1.3. Vessel anatomy, structure and function**

Arteries are blood vessels that transport oxygenated blood to the whole body from the heart (except for the pulmonary artery, which carries deoxygenated blood to the lungs).

There are three types of arteries. The elastic or conducting arteries have a thick media layer to resist the pulses of the heart. The aorta stands out as the largest artery that carries blood from the heart to the rest (with a diameter ranging from 2 to 4 cm). Then, the muscular arteries are medium-sized and carry blood from elastic arteries, and eventually branch into arterioles. Finally, arterioles deliver blood to a large number of capillaries (it is estimated that there are more than 40,000 kilometers of capillaries in an adult) (Iaizzo, 2015).

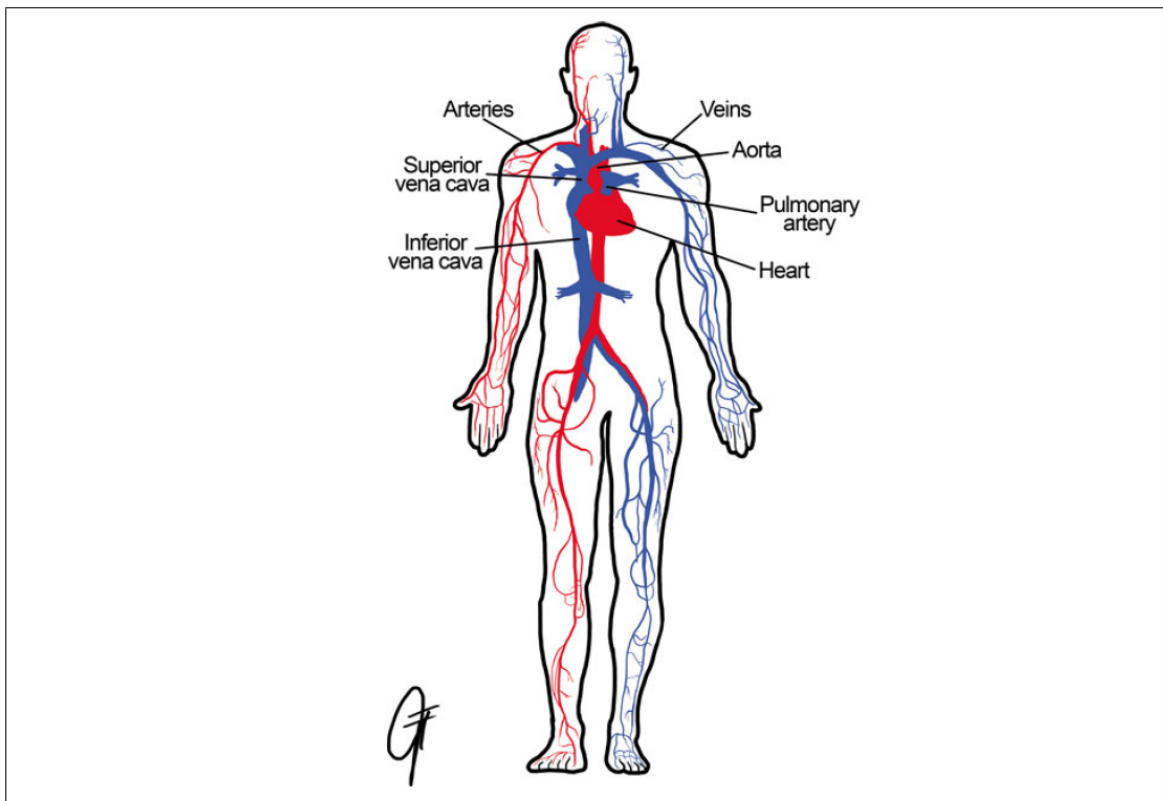


Figure 1.3. The major components of the cardiovascular system: circulating blood, the blood vessels, and the heart. Taken and modified from Iaizzo (2015)

From an anatomical point of view, each artery is a muscular tube lined with smooth tissue and composed of three main layers: the intima, the media, and the adventitia (see figure 1.4). The intima (tunica intima) is the innermost layer of blood vessels. In young and healthy subjects, the intima is typically thin and does not contribute significantly to the overall mechanical response. The media (tunica media) is the thicker layer of the artery wall. It comprises a complex fibrous network of smooth muscle cells, collagen fibers, and elastin. These fibers distribute helically into two groups, which present a small pitch and a defined orientation. The adventitia (tunica adventitia) is the external layer of the artery wall. It consist of dispersed fibroblasts and fibrocytes, histological ground substance, and fibrous tissue, formed by collagen fibrils arranged in thick bundles. The thickness of the adventitia is highly conditioned by the type of artery (muscular or elastic), its function, and its location (Holzapfel et al., 2000). The mechanical contribution of the adventitia is to serve as an additional reinforcement to the wall, which stops the artery from overstretching and rupture (O. R. W. . H. G. A. Gasser T. C., 2006).

#### 1.4. Notions of Continuum Mechanics

The aim of continuum mechanics is to describe the motion and deformation of a body. In the following we use uppercase and lowercase symbols for undeformed (initial) and deformed (current) configurations, respectively. In this context, the coordinates of the particles of a continuum body  $\Omega$  in the time  $t$  can be described by

$$\mathbf{x} = \boldsymbol{\varphi}(\mathbf{X}, t) \quad \forall \mathbf{X} \in \Omega_0, \quad (1.1)$$

where the undeformed configuration of the body is represented by  $\Omega_0$ , and  $\boldsymbol{\varphi}$  is a function that describes the motion, commonly known as the deformation mapping or motion mapping. Consequently, the displacement field can be defined as

$$\mathbf{U} = \mathbf{x} - \boldsymbol{\varphi}(\mathbf{X}, t) \quad \forall \mathbf{X} \in \Omega_0. \quad (1.2)$$

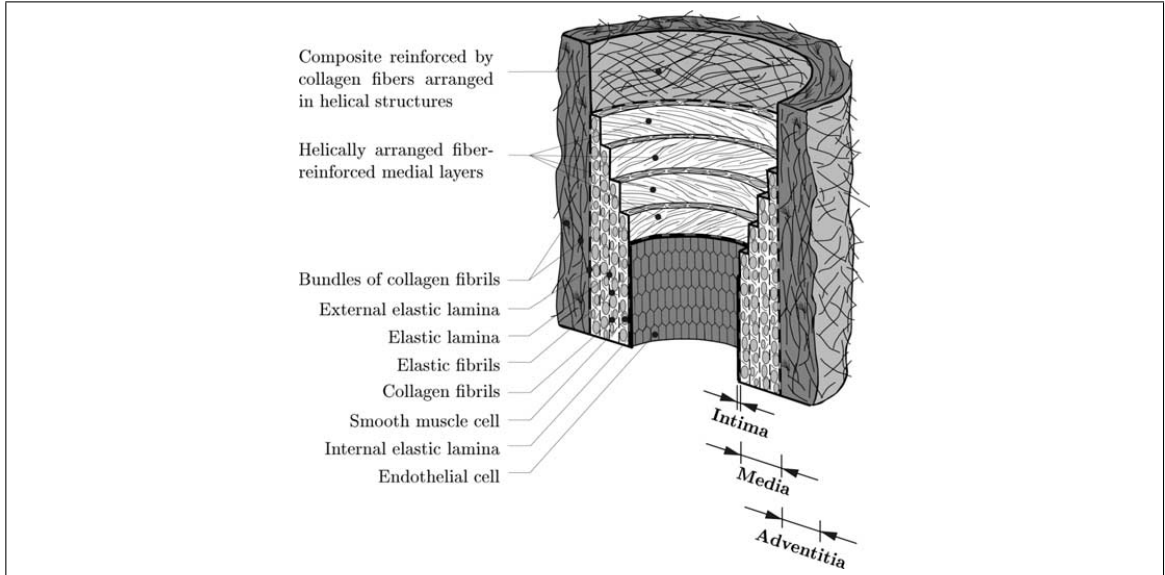


Figure 1.4. Artery anatomy showing the major components of a healthy artery. Taken from Holzapfel et al. (2000).

Let be  $d\mathbf{X}$  be a infinitesimal vector at a point  $\mathbf{x}$  in the undeformed configuration  $\Omega_0$ , which is mapped by  $\varphi(\mathbf{X}, t)$  to an infinitesimal vector  $d\mathbf{x}$  at time  $t$  in the current configuration. Based on these definitions, we can establish a relation between  $d\mathbf{X}$  and  $d\mathbf{x}$  by

$$d\mathbf{x} = \mathbf{F}d\mathbf{X} \quad (1.3)$$

where  $\mathbf{F} = \nabla_0\varphi(\mathbf{X}, t)$  is the deformation gradient tensor. The deformation gradient tensor delivers all the information needed to assess deformation during the motion of a continuum body. For example, the determinant of  $\mathbf{F}$  is used to measure the volumetric change caused by the motion

$$J = \det(\mathbf{F}) \quad (1.4)$$

Further, the right Cauchy-Green tensor  $\mathbf{C}$  is employed calculate deformations into a body and is defined by

$$\mathbf{C} = \mathbf{F}^T\mathbf{F}. \quad (1.5)$$

The Cauchy stress tensor  $\boldsymbol{\sigma}$  represent the stress state in each point inside the body during the motion, and relates the unit vector  $\boldsymbol{n}$  to the surface traction  $\boldsymbol{t}$  in the deformed configuration. This tensor is defined by

$$\boldsymbol{t} = \boldsymbol{\sigma} \cdot \boldsymbol{n}. \quad (1.6)$$

The first Piola-Kirchhoff stress tensor  $\boldsymbol{P}$  is useful for the measurement of stresses in the reference configuration. This quantity is related with the Cauchy stress tensor by

$$\boldsymbol{P} = J\boldsymbol{\sigma}\boldsymbol{F}^{-T}. \quad (1.7)$$

Finally, the second Piola-Kirchhoff stress tensor  $\boldsymbol{S}$  describes the stress in the reference configuration with respect to the unit area in the undeformed state, and is defined by

$$\boldsymbol{S} = \boldsymbol{F}^{-1}\boldsymbol{P} \quad (1.8)$$

With the deformation and stress tensors defined, we can state the non-linear elasticity problem as follows: Find the deformation mapping  $\boldsymbol{\varphi} : \Omega_0 \rightarrow \mathbb{R}^3$  such that

$$\begin{cases} \text{Div } \boldsymbol{P} + \boldsymbol{B} = \mathbf{0} & \text{in } \Omega_0, \\ \boldsymbol{P} \cdot \boldsymbol{N} = \boldsymbol{T} & \text{on } \partial\Omega_0^N, \\ \boldsymbol{\varphi} = \bar{\boldsymbol{\varphi}} & \text{on } \partial\Omega_0^D. \end{cases} \quad (1.9)$$

Here,  $\boldsymbol{N}$  is the unitary normal vector,  $\boldsymbol{T}$  represents the surface forces per unit area acting on  $\partial\Omega_0^N$ , and  $\bar{\boldsymbol{\varphi}}$  is the prescribed displacement on  $\partial\Omega_0^D$ . Additionally, the incompressible condition can be set by incorporating the constraint

$$J = 1 \quad \text{in } \Omega_0. \quad (1.10)$$

Finally, a constitutive relationship between the deformation tensors and the stress tensors needs to be defined.

## 1.5. Cardiac tissue constitutive modeling

Simulations of the heart function require that (i) the underlying model reproduces the geometry in the most realistic way possible, (ii) the balance laws must hold, and boundary conditions must represent realistic physiological conditions, and (iii) the constitutive relation must reproduce the mechanical behavior of the myocardium. Heart models are commonly constructed over geometrical data acquired *in vivo* and using computed tomography or MRI. If no structural information is available, the fiber orientation can be approximated or mapped from an rule-based algorithms. Typically, the fiber orientation is assigned to heart models by using techniques as Diffusion Tensor Imaging (DTI). However, other algorithms, such as the Laplace–Dirichlet Rule-Based (LDRB), are available (Bayer et al., 2012).

From a mechanical point of view, since the early 1900s, the heart tissue has been understood as if it made up of bundles of muscle fibers arranged in a single layer helical wound around the ventricles (MacCallum, 1900). Following this path, various constitutive models and numerical simulations of the myocardium have been performed and are available in the literature. Using a continuum framework, the first models of passive myocardium took into account of its fibrous microstructure. They considered it an incompressible and transversely isotropic material with a Fung-type constitutive relation developed by Guccione and its collaborators (Fung, 1993; Guccione, McCulloch, & Waldman, 1991), where the strain energy density is written as

$$W(\varphi) = \frac{c}{2} (\exp\{Q\} - 1), \quad (1.11)$$

where

$$Q = b_f E_{11}^2 + b_t (E_{22}^2 + E_{33}^2 + E_{23}^2 + E_{32}^2) + b_{fs} (E_{12}^2 + E_{21}^2 + E_{13}^2 + E_{31}^2), \quad (1.12)$$

and  $E_{ij}$  are the components of the Green - Lagrange strain tensor.

More recently, models have incorporated anisotropies that consider the myocardium as a continuum material formed of interconnected sheets with fibers aligned with a preferred orientation. One popular model for the passive myocardial tissue response was developed by Holzapfel and collaborators, and is entirely invariant-based, orthotropic, convex (Holzapfel & Ogden, 2009; Göktepe et al., 2011). This strain energy density function is written as

$$W(\mathbf{F}) = \sum_{j=1,4f,4s,8fs} \frac{a_j}{2b_j} \{ \exp (b_j \{I_j(\mathbf{F}) - \beta_j\}^{\gamma_j}) - \alpha_j \}, \quad (1.13)$$

where where,  $I_i$  are the invariants of the right Cauchy-Green tensor,  $a_i$  and  $b_i$  are material constants, and  $\alpha_1 = 3$ ,  $\alpha_{4f} = 1$ ,  $\alpha_{4s} = 1$ ,  $\alpha_{8fs} = 0$ ,  $\beta_1 = 3$ ,  $\beta_{4f} = 1$ ,  $\beta_{4s} = 1$ ,  $\beta_{8fs} = 0$ ,  $\gamma_1 = 1$ ,  $\gamma_{4f} = 2$ ,  $\gamma_{4s} = 2$ , and  $\gamma_{8fs} = 2$ .

## 1.6. Artery tissue constitutive modeling

In order to allow investigation and the assessment of the mechanical behavior of the great vessels, various numerical simulations have been performed (Chuong & Fung, 1983; Hunter & Smaill, 1988; García-Herrera & Celentano, 2013). The artery has been typically modeled as a thick-walled, orthotropic, and nonlinear elastic hollow cylinder, which considers the media and adventitia layers (the solid mechanically relevant layers in healthy tissue). These models have been tested under loading protocols that can include inflation, stretching, and residual stresses. It is relevant to consider that an artery *in vivo* is a pre-stretched material under an internal pressure load. Meanwhile, for artery *in vitro*, the residual stress is typically incorporated by assuming that the natural (unstressed and unstrained) configuration corresponds to an open section of a tube, which is then closed by an initial bending to form a load-free, but stressed, cylinder before the application of the

loading protocol (Vossoughi, 1993; J. Humphrey, 1995; Holzapfel et al., 2000). Several

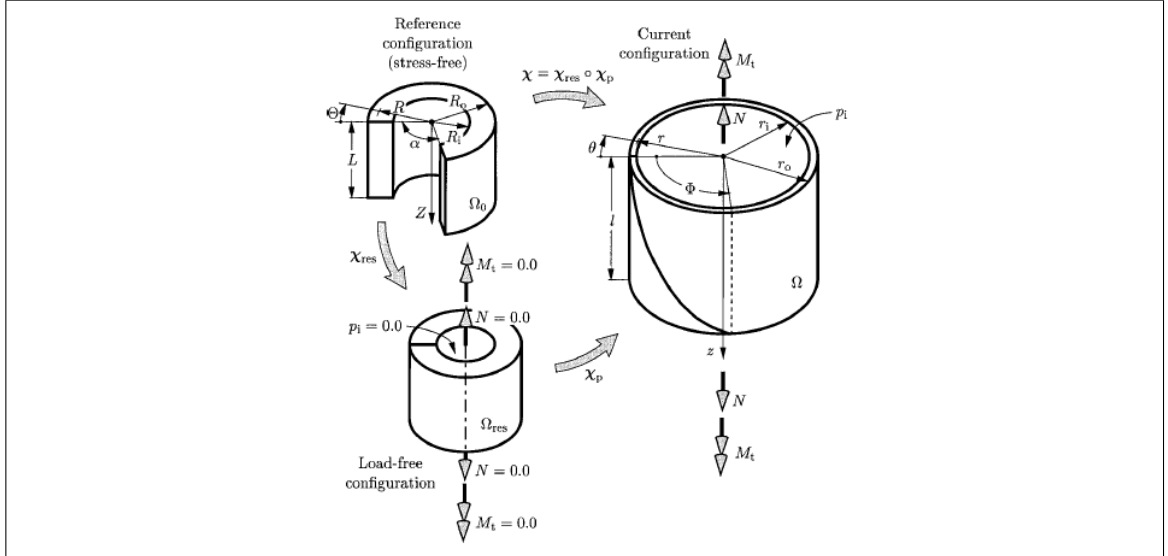


Figure 1.5. Schematic representation of the residual stresses. Figure shows a segment of an artery in the (stress-free), in the load-free configuration, and in the current configuration. Taken from Holzapfel et al. (2000).

formulations for artery wall simulations have been proposed in the literature. The majority of the constitutive models are phenomenological, and do not take directly into account the microstructural arrangement and compounds of the cardiac tissue. Other approaches are available in the literature, including isotropic formulations, as in Delfino *et al.* (Delfino, Stergiopoulos, Moore, & Meister, 1997), whose strain energy density function is written as

$$W[\varphi] = \frac{a}{b} \left\{ \exp \left( \frac{b}{2} \{ I_1 - 3 \} \right) \right\}, \quad (1.14)$$

where  $a$  and  $b$  are material parameters and  $I_1$  is the first invariant of the right Cauchy-Green tensor.

Holzappel *et al.* introduced another more realistic formulation, an orthotropic model constructed upon a two-layer geometry (Holzapfel et al., 2000). Here, each layer is treated as fiber-reinforced material with the fibers symmetrically disposed around the cylinder axis. The corresponding strain energy density function is described by the expression

$$W[\varphi] = \frac{c_1}{2} \{(I_1 - 3)\} + \sum_{i=4,6} \frac{k_1}{2k_2} \{\exp\{k_2 (I_i - 1)^2\} - 1\}, \quad (1.15)$$

where  $I_1, I_4$  and  $I_6$  are the invariants of the right Cauchy-Green tensor, and  $c_1, k_1$  and  $k_2$  are material parameters.

## **2. ACCELERATING CARDIAC AND VESSEL MECHANICS SIMULATIONS: AN ENERGY TRANSFORMED VARIATIONAL FORMULATION FOR HYPERELASTIC BIOSOLIDS**

### **2.1. Introduction**

Mathematical models and computer simulations of human organs provide a powerful framework for in-silico experimentation in cardiovascular research and translational medicine (Winslow et al., 2012; Quarteroni et al., 2017). Based on the framework of continuum mechanics, researchers have studied the mechanical response of the heart chambers to passive filling, and the deformation processes taking place in arterial walls due to pulsatile blood flow (Hunter & Smaill, 1988; Chuong & Fung, 1983). Current models for cardiac muscles and arterial walls have strongly benefited from the theory of hyperelasticity, as these tissues undergo large deformations, display a non-linear constitutive response, and behave as incompressible or near-incompressible materials (Guccione et al., 1991; Holzapfel et al., 2000; Chagnon, Rebouah, & Favier, 2015). These material features, combined with a kinematic framework that accounts for finite deformations, result in non-linear variational formulations that are approximately solved employing non-linear finite-element (FE) analysis (Nash & Hunter, 2001; Nordsletten, Niederer, Nash, Hunter, & Smith, 2011). Cardiovascular models that follow this approach have remarkable applications in understanding the remodeling process occurring in the cardiac chambers of failing hearts under novel treatments (Wall, Walker, Healy, Ratcliffe, & Guccione, 2006), as well as in the assessment of the loading conditions that result in the rupture of aneurysms (T. Gasser, Auer, Labruto, Swedenborg, & Roy, 2010), among many others.

While numerical simulations have proved successful in predicting the biomechanical function of the heart and the great vessels, one outstanding challenge is the reduction of the computing time that these simulations can take. This computational burden can

be attributed to many sources. First, the numerical precision sought by the analyst or required by physical and analytical considerations drives the level of spatial and temporal discretization (Pezzuto, Hake, & Sundnes, 2016; Hurtado & Rojas, 2018). These requirements translate into fine meshes and small time-steps that directly increase the number of degrees of freedom (DOFs) in the non-linear system of equations and the number of time-step iterations. Second, the underlying non-linear system of equations is typically solved using iterative methods (e.g., Newton's method), where linearization of the residual leads to a series of linear systems of equations (Göktepe et al., 2011; Sundnes, Wall, Osnes, Thorvaldsen, & McCulloch, 2012). At each iteration, residuals and tangents need to be computed and assembled, increasing the computing time with the number of steps needed to meet some error criteria. Third, the solution of linear systems of equations with millions of DOFs, where direct methods are suboptimal and iterative methods of numerical linear algebra are preferred (Saad & Schultz, 1986).

Several strategies have been proposed in the literature to alleviate the computational burden found in biomechanical simulations. From a theoretical perspective, heart simulations assuming quasi-incompressible and fully-incompressible tissue models problems have been addressed using mixed formulations and FE discretizations (Göktepe et al., 2011; Hadjicharalambous, Lee, Smith, & Nordsletten, 2014). In all cases, they have efficiently reduced the computing time by alleviating the volumetric locking phenomenon, a method with a demonstrated history of success in computational mechanics (Malkus & Hughes, 1978; Simo, Taylor, & Pister, 1985). From a computer architecture perspective, the parallelization of non-linear FE codes in high-performance computing (HPC) platforms has been critical in reducing the wall-clock time of biomechanical simulations (Lafortune et al., 2012; Augustin, Holzapfel, & Steinbach, 2014). For example, computational models of heart mechanics have been implemented in GPU architectures, resulting in up to two-fold speed-ups compared to multi-core CPU alternatives (Vigueras

et al., 2014). A complementary strategy to accelerate cardiac simulations is the use of advanced preconditioners from numerical linear algebra to improve the performance of iterative solvers in the solution of linear system of equations (Campos, dos Santos, Sundnes, & Rocha, 2018). A more recent approach considers transforming the residual equations that arise in non-linear FE discretizations of the principle of virtual works (Mei, Hurtado, Pant, & Aggarwal, 2018). The solution of the transformed problem results in a notable reduction in the number of iterations needed to achieve the desired convergence tolerance, allowing the use of larger load steps than those employed in traditional numerical schemes. This method has proven to be very efficient for regular geometries under simple loading conditions. However, its applicability to generalized problems in cardiovascular mechanics remains open, as the choice of the transformation, and in turn, the success of the method strongly depends on the type of loading.

In this work, we introduce a novel energy-transform variational formulation (ETVF) that effectively accelerates the solution of numerical simulations of soft-tissue mechanics. We start by presenting a mixed variational framework where we introduce auxiliary invariant-based fields that render the strain energy density into a quadratic form, see Section 2.2. In addition, we consider a function transformation of the auxiliary-field constraints in the variational formulation that reduce the degree of non-linearity of the problem. In Section 2.3, we use multi-field FE discretizations to solve the ETVF of standard problems in cardiac and vessel mechanics. We also assess the numerical performance of the ETVF compared to standard FE methods in an anatomically-detailed model of a human heart under passive filling that assumes an orthotropic heterogeneous non-linear constitutive relation. We end by discussing the accuracy and numerical performance of the ETVF models and explaining why it delivers important speed-ups in computing time in Section 2.4, together with providing future perspectives of our work.

## 2.2. Energy-transformed variational formulation of the hyperelastic problem and finite-element discretization

### 2.2.1. Standard variational formulations for the quasi-incompressible and incompressible hyperelasticity problems

In the following, we adopt a continuum approach to describe the mechanical behavior of the heart, see, for example, (J. D. Humphrey, 2002). Let  $\Omega_0 \subset \mathbb{R}^3$  be the cardiac domain in the reference (material) configuration. We will be interested in finding a deformation mapping  $\varphi : \Omega_0 \rightarrow \mathbb{R}^3$  that maps material points  $\mathbf{X}$  in the reference configuration to the current (spatial) configuration  $\Omega = \varphi(\Omega_0)$ . In the current configuration, the body is assumed to be in equilibrium, a balance statement that can be written in terms of the mechanical equilibrium equations

$$\text{Div } \mathbf{P} + \mathbf{B} = \mathbf{0} \quad \text{in } \Omega_0, \quad (2.1)$$

where  $\mathbf{P} : \Omega_0 \rightarrow \mathbb{R}^{3 \times 3}$  is the first Piola-Kirchhoff (PK1) stress tensor field, and  $\mathbf{B} : \Omega_0 \rightarrow \mathbb{R}^3$  is the material body force density per unit volume. Adopting a thermomechanical framework, the constitutive relation defining the PK1 stress tensor takes the form

$$\mathbf{P}(\mathbf{F}) := \frac{\partial W}{\partial \mathbf{F}}, \quad (2.2)$$

where  $W : \mathbb{R}^{3 \times 3} \rightarrow \mathbb{R}$  is the strain energy density, and  $\mathbf{F} := \nabla \varphi$  is the deformation-gradient tensor. The boundary of the reference configuration is partitioned into a Dirichlet boundary  $\partial\Omega_0^D$  where displacements are prescribed, i.e.

$$\varphi = \bar{\varphi} \quad \text{on } \partial\Omega_0^D, \quad (2.3)$$

and into a Neumann boundary  $\partial\Omega_0^N$  where tractions are prescribed, i.e.,

$$\mathbf{P}\mathbf{N} = \bar{\mathbf{T}} \quad \text{on } \partial\Omega_0^N, \quad (2.4)$$

where  $\mathbf{N}$  is the normal vector at the boundary,  $\bar{\varphi}$  and  $\bar{T}$  are functions that describe the Dirichlet and Neumann boundary conditions, respectively, and we note that  $\partial\Omega_0 = \partial\Omega_0^D \cup \partial\Omega_0^N$ . Equations (2.1),(2.2),(2.3), and (2.4) constitute the classical hyperelasticity boundary value problem used in cardiac and vessel mechanics problems (J. D. Humphrey, 2002).

An alternative and equivalent formulation of the hyperelasticity problem can be expressed in terms of variational problems (Ogden, 1997). To this end, we define the trial space

$$\mathcal{S}_0 := \{ \mathbf{w} \in H^1(\Omega_0, \mathbb{R}^3) \text{ such that } \mathbf{w} = \bar{\varphi} \text{ on } \partial\Omega_0^D \}, \quad (2.5)$$

and the corresponding test space

$$\mathcal{V}_0 := \{ \mathbf{v} \in H^1(\Omega_0, \mathbb{R}^3) \text{ such that } \mathbf{v} = \mathbf{0} \text{ on } \partial\Omega_0^D \}, \quad (2.6)$$

where  $H^1(\Omega_0, \mathbb{R}^3)$  is the Sobolev space of functions. Further, we define the potential energy functional

$$\Pi[\mathbf{w}] = \int_{\Omega_0} W(\nabla_0 \mathbf{w}) - \int_{\Omega_0} \mathbf{w} \cdot \mathbf{B} - \int_{\partial\Omega_0^N} \mathbf{w} \cdot \bar{\mathbf{T}}. \quad (2.7)$$

Then, the variational formulation of the hyperelasticity problem takes the following form:

Find  $\varphi \in \mathcal{S}_0$  such that

$$\Pi[\varphi] = \min_{\mathbf{w} \in \mathcal{S}_0} \Pi[\mathbf{w}]. \quad (2.8)$$

A standard approach in solving the hyperelasticity problem for quasi-incompressible tissues is to adopt a mixed Hu-Washizu formulation (Bonet & Wood, 2008). To this end, we employ a deviatoric-volumetric decomposition of the deformation gradient tensor, and rewrite the strain energy density as

$$\hat{W}(\mathbf{F}, J) := W(\det(\mathbf{F})^{-1/3} \mathbf{F}) + U(J), \quad (2.9)$$

where  $U : \mathbb{R} \rightarrow \mathbb{R}$  is the bulk energy density, typically taken as  $U(J) = \frac{1}{2}\kappa \{J - 1\}^2$ . Further, we set the space

$$\mathcal{P}_0 := \{\eta \in L^2(\Omega_0, \mathbb{R})\}, \quad (2.10)$$

and we define the Hu-Washizu energy functional by

$$Q[\mathbf{w}, q, \omega] := \int_{\Omega_0} \hat{W}(\nabla_0 \mathbf{w}, \omega) - \int_{\Omega_0} \mathbf{w} \cdot \mathbf{B} - \int_{\partial\Omega_0^N} \mathbf{w} \cdot \bar{\mathbf{T}} - \int_{\Omega_0} \{\det \nabla_0 \mathbf{w} - \omega\} q. \quad (2.11)$$

Then, the Hu-Washizu variational formulation reads: Find  $\varphi \in \mathcal{S}_0$ ,  $p \in \mathcal{P}_0$  and  $\theta \in \mathcal{P}_0$  such that

$$Q[\varphi, p, \theta] := \min_{\mathbf{w} \in \mathcal{S}_0} \max_{q, \xi \in \mathcal{P}_0} Q[\mathbf{w}, q, \xi]. \quad (2.12)$$

Stationary conditions associated to problem (2.12) result in the weak form of the quasi-incompressible hyperelasticity problem: Find  $\varphi \in \mathcal{S}_0$ ,  $p \in \mathcal{P}_0$  and  $\theta \in \mathcal{P}_0$  such that

$$D_{\mathbf{v}} Q[\varphi, p, \theta] = \int_{\Omega_0} \left\{ \frac{\partial \hat{W}}{\partial \mathbf{F}}(\nabla_0 \varphi, \theta) - p \det(\nabla_0 \varphi) (\nabla_0 \varphi)^{-T} \right\} : \nabla_0 \mathbf{v} - \int_{\Omega_0} \mathbf{v} \cdot \mathbf{B} - \int_{\partial\Omega_0^T} \mathbf{v} \cdot \bar{\mathbf{T}} = 0, \quad \forall \mathbf{v} \in \mathcal{V}_0, \quad (2.13)$$

$$D_q Q[\varphi, p, \theta] = \int_{\Omega_0} \{\det(\nabla_0 \varphi) - \theta\} q = 0, \quad \forall q \in \mathcal{P}_0, \quad (2.14)$$

$$D_\omega Q[\varphi, p, \theta] = \int_{\Omega_0} \left\{ \frac{\partial U}{\partial J}(\theta) + p \right\} \omega = 0, \quad \forall \omega \in \mathcal{P}_0. \quad (2.15)$$

We now focus in the case where tissue behaves as an incompressible material. To model this behavior, the following kinematic restriction on local volume change must hold:

$$\det(\nabla_0 \varphi) = 1 \quad \text{in } \Omega_0. \quad (2.16)$$

The incompressibility constraint posed by (2.16) can be introduced in the variational formulation using the method of Lagrange multipliers. We define the Lagrangian by

$$I[\mathbf{w}, q] := \Pi[\mathbf{w}] - \int_{\Omega_0} \{\det(\nabla_0 \mathbf{w}) - 1\} q. \quad (2.17)$$

Then, the mixed formulation for the incompressible hyperelasticity problem reads: Find  $\varphi \in \mathcal{S}_0$  and  $p \in \mathcal{P}_0$  such that

$$I[\varphi, p] = \min_{\mathbf{w} \in \mathcal{S}_0} \max_{q \in \mathcal{P}_0} I[\mathbf{w}, q]. \quad (2.18)$$

Stationary conditions for the variational problem (2.18) deliver the weak form for the incompressible hyperelasticity problem: Find  $\varphi \in \mathcal{S}_0$  and  $p \in \mathcal{P}_0$  such that

$$\begin{aligned} D_{\mathbf{v}} I[\varphi, p] = \int_{\Omega_0} \left\{ \frac{\partial W}{\partial \mathbf{F}}(\nabla_0 \varphi) - p \det(\nabla_0 \varphi) (\nabla_0 \varphi)^{-T} \right\} : \nabla_0 \mathbf{v} \\ - \int_{\Omega_0} \mathbf{v} \cdot \mathbf{B} - \int_{\partial \Omega_0^T} \mathbf{v} \cdot \bar{\mathbf{T}} = 0, \quad \forall \mathbf{v} \in \mathcal{V}_0, \end{aligned} \quad (2.19)$$

$$D_q I[\varphi, p] = \int_{\Omega_0} \{\det(\nabla_0 \varphi) - 1\} q = 0, \quad \forall q \in \mathcal{P}_0. \quad (2.20)$$

### 2.2.2. Energy-transform variational formulations for the hyperelasticity problem

In the following, we present a family of energy-transformed variational formulations (ETVF) for vessel and cardiac mechanics. To this end, we introduce auxiliary fields that are constructed upon the particular expression for the strain energy density, such that a simple transformation allows to reduce the degree of non-linearity of the objective function to be minimized. To this end, we start by assuming that the strain energy density has the general form

$$W(\mathbf{F}) = \sum_{j=1}^m \frac{c_j}{2} \{f_j(\mathbf{F}) - \alpha_j\},$$

where  $c_j, \alpha_j, j = 1, \dots, m$  are positive constants, and  $f_j : \mathbb{R}^{3 \times 3} \rightarrow \mathbb{R}, j = 1, \dots, m$  are functions typically based on invariants of  $\mathbf{F}$ . We define auxiliary variables  $\eta_j$  such that  $\eta_j^2 = f_j(\mathbf{F})$  for  $j = 1, \dots, m$  and look for bijective transformation  $g_j : \mathbb{R} \rightarrow \mathbb{R}$  such that

the constraint associated to auxiliary variables can be written as

$$g_j(\eta_j^2) - g_j(f_j(\mathbf{F})) = 0, \quad j = 1 \dots, m. \quad (2.21)$$

Transformed constraint equations (2.21) are expected to have a lower degree of non-linearity than that of function  $f_j$ . In this way, we use a Lagrange multiplier approach, where the energy density of the Lagrangian functional takes the form

$$\tilde{W}(\mathbf{F}, \boldsymbol{\eta}, \boldsymbol{\xi}) = \sum_{j=1}^m \frac{c_j}{2} \{\eta_j^2 - \alpha_j\} - \sum_{j=1}^m \{g_j(\eta_j^2) - g_j(f_j(\mathbf{F}))\} \xi_j, \quad (2.22)$$

where  $\boldsymbol{\eta} = [\eta_1, \dots, \eta_m]$ , and  $\boldsymbol{\xi} = [\xi_1, \dots, \xi_m]$ . Then, for the case of quasi-incompressible hyperelasticity, the Lagrangian reads

$$\begin{aligned} \tilde{Q}[\mathbf{v}, q, \omega, \boldsymbol{\eta}, \boldsymbol{\xi}] = & \int_{\Omega_0} \sum_{j=1}^m \left\{ \frac{c_j}{2} \{\eta_j^2 - \alpha_j\} - \{g_j(\eta_j^2) - g_j(f_j(\det(\nabla_0 \mathbf{v}))^{-1/3} \nabla_0 \mathbf{v}))\} \xi_j \right\} \\ & - \int_{\Omega_0} U(\omega) + \{\det(\nabla_0 \mathbf{v}) - \omega\} q - \int_{\Omega_0} \mathbf{v} \cdot \mathbf{B} - \int_{\partial \Omega_0^N} \mathbf{v} \cdot \bar{\mathbf{T}}. \end{aligned} \quad (2.23)$$

Based on this framework, and defining the space  $\mathcal{P}_0^m := \underbrace{\mathcal{P}_0 \times \dots \times \mathcal{P}_0}_{m\text{-times}}$ , the ETVF for the quasi-incompressible hyperelasticity problem reads: Find  $\boldsymbol{\varphi} \in \mathcal{S}_0$ ,  $p \in \mathcal{P}_0$ ,  $\theta \in \mathcal{P}_0$ ,  $\boldsymbol{\phi} \in \mathcal{P}_0^m$  and  $\boldsymbol{\lambda} \in \mathcal{P}_0^m$  such that

$$\tilde{Q}[\boldsymbol{\varphi}, p, \theta, \boldsymbol{\phi}, \boldsymbol{\lambda}] = \min_{\boldsymbol{v} \in \mathcal{S}_0} \max_{q, \omega \in \mathcal{P}_0, \boldsymbol{\eta}, \boldsymbol{\xi} \in \mathcal{P}_0^m} \tilde{Q}[\mathbf{v}, q, \omega, \boldsymbol{\eta}, \boldsymbol{\xi}]. \quad (2.24)$$

Stationary conditions for (2.24) take the form

$$\begin{aligned} D_{\mathbf{v}} \tilde{Q}[\boldsymbol{\varphi}, p, \theta, \boldsymbol{\phi}, \boldsymbol{\lambda}] = & \int_{\Omega_0} \hat{\mathbf{P}}(\nabla_0 \boldsymbol{\varphi}, \lambda, p) : \nabla_0 \mathbf{v} - \int_{\Omega_0} \mathbf{v} \cdot \mathbf{B} \\ & - \int_{\partial \Omega_0^N} \mathbf{v} \cdot \bar{\mathbf{T}} = 0, \quad \forall \mathbf{v} \in \mathcal{V}_0, \end{aligned} \quad (2.25)$$

$$D_q \tilde{Q}[\boldsymbol{\varphi}, p, \theta, \boldsymbol{\phi}, \boldsymbol{\lambda}] = \int_{\Omega_0} \{\det(\nabla_0 \boldsymbol{\varphi}) - \theta\} q = 0, \quad \forall q \in \mathcal{P}_0, \quad (2.26)$$

$$D_\omega \tilde{Q}[\boldsymbol{\varphi}, p, \theta, \boldsymbol{\phi}, \boldsymbol{\lambda}] = \int_{\Omega_0} \{U'(\theta) - p\} \omega = 0, \quad \forall \omega \in \mathcal{P}_0, \quad (2.27)$$

$$D_{\boldsymbol{\eta}} \tilde{Q}[\boldsymbol{\varphi}, p, \theta, \boldsymbol{\phi}, \boldsymbol{\lambda}] = \int_{\Omega_0} \sum_{j=1}^m \left\{ c_j \phi_j - 2 \frac{\partial g_j}{\partial x} (\phi_j^2) \phi_j \lambda_j \right\} \eta_j = 0, \quad \forall \boldsymbol{\eta} \in \mathcal{P}_0^m, \quad (2.28)$$

$$D_{\boldsymbol{\xi}} \tilde{Q}[\boldsymbol{\varphi}, p, \theta, \boldsymbol{\phi}, \boldsymbol{\lambda}] = \int_{\Omega_0} \sum_{j=1}^m \left\{ g_j(\eta_j^2) - g_j(f_j(\det(\nabla_0 \boldsymbol{\varphi})^{-1/3} \nabla_0 \boldsymbol{\varphi})) \right\} \xi_j = 0, \quad \forall \boldsymbol{\xi} \in \mathcal{P}_0^m, \quad (2.29)$$

where we define

$$\begin{aligned} \hat{\mathbf{P}}(\mathbf{F}, \lambda, p) := \\ \sum_{j=1}^m \left\{ \frac{\partial g_j}{\partial x} (f_j(\det(\mathbf{F})^{-1/3} \mathbf{F})) \frac{\partial f_j}{\partial \det(\mathbf{F})^{-1/3} \mathbf{F}}(\mathbf{F}) \left\{ -\frac{1}{3} \mathbf{F}^{-T} + \mathbf{I} \right\} \lambda_j \right\} - p \det(\mathbf{F}) \mathbf{F}^{-T}. \end{aligned} \quad (2.30)$$

Similarly, for the case of incompressible hyperelasticity, we consider the Lagrangian

$$\begin{aligned} \tilde{I}[\mathbf{v}, q, \boldsymbol{\eta}, \boldsymbol{\xi}] := \int_{\Omega_0} \left\{ \sum_{j=1}^m \frac{c_j}{2} \{\eta_j^2 - \alpha_j\} - \sum_{j=1}^m \{g_j(\eta_j^2) - g_j(f_j(\nabla_0 \mathbf{v}))\} \xi_j \right\} \\ - \int_{\Omega_0} \{\det(\nabla_0 \mathbf{v}) - 1\} q - \int_{\Omega_0} \mathbf{v} \cdot \mathbf{B} - \int_{\partial \Omega_0^N} \mathbf{v} \cdot \bar{\mathbf{T}}. \end{aligned} \quad (2.31)$$

Then, the ETVF for the incompressible hyperelasticity problem takes the form: Find  $\boldsymbol{\varphi} \in \mathcal{S}_0$ ,  $p \in \mathcal{P}_0$ ,  $\boldsymbol{\phi} \in \mathcal{P}_0^m$  and  $\boldsymbol{\lambda} \in \mathcal{P}_0^m$  such that

$$\tilde{I}[\boldsymbol{\varphi}, p, \boldsymbol{\phi}, \boldsymbol{\lambda}] = \min_{\mathbf{v} \in \mathcal{S}_0} \max_{q \in \mathcal{P}_0, \boldsymbol{\eta}, \boldsymbol{\xi} \in \mathcal{P}_0^m} \tilde{I}[\mathbf{v}, q, \boldsymbol{\eta}, \boldsymbol{\xi}], \quad (2.32)$$

and the associated stationary conditions result in the weak equations

$$D_{\mathbf{v}} \tilde{I}[\boldsymbol{\varphi}, p, \boldsymbol{\phi}, \boldsymbol{\lambda}] = \int_{\Omega_0} \tilde{\mathbf{P}}(\nabla_0 \boldsymbol{\varphi}, \boldsymbol{\lambda}, p) : \nabla_0 \mathbf{v} - \int_{\Omega_0} \mathbf{v} \cdot \mathbf{B} - \int_{\partial\Omega_0^N} \mathbf{v} \cdot \bar{\mathbf{T}} = 0, \quad \forall \mathbf{v} \in \mathcal{V}_0, \quad (2.33)$$

$$D_q \tilde{I}[\boldsymbol{\varphi}, p, \boldsymbol{\phi}, \boldsymbol{\lambda}] = \int_{\Omega_0} \{\det(\nabla_0 \boldsymbol{\varphi}) - 1\} q = 0, \quad \forall q \in \mathcal{P}_0, \quad (2.34)$$

$$D_{\boldsymbol{\eta}} \tilde{I}[\boldsymbol{\varphi}, p, \boldsymbol{\phi}, \boldsymbol{\lambda}] = \int_{\Omega_0} \sum_{j=1}^m \left\{ c_j \phi_j - 2 \frac{\partial g_j}{\partial x} (\phi_j^2) \phi_j \lambda_j \right\} \eta_j = 0, \quad \forall \boldsymbol{\eta} \in \mathcal{P}_0^m, \quad (2.35)$$

$$D_{\boldsymbol{\xi}} \tilde{I}[\boldsymbol{\varphi}, p, \boldsymbol{\phi}, \boldsymbol{\lambda}] = \int_{\Omega_0} \sum_{j=1}^m \{g_j(\eta_j^2) - g_j(f_j(\nabla_0 \mathbf{v}))\} \xi_j = 0, \quad \forall \boldsymbol{\xi} \in \mathcal{P}_0^m, \quad (2.36)$$

where

$$\tilde{\mathbf{P}}(\mathbf{F}, \boldsymbol{\lambda}, p) := \sum_{j=1}^m \left\{ \frac{\partial g_j}{\partial x} (f_j(\mathbf{F})) \frac{\partial f_j}{\partial \mathbf{F}}(\mathbf{F}) \boldsymbol{\lambda} - p \det(\mathbf{F}) \mathbf{F}^{-T} \right\}. \quad (2.37)$$

In the following, we apply the ETVF framework to standard models of cardiac and vessel mechanics.

### 2.2.2.1. ETVF for a transversely-isotropic exponential model for cardiac tissue

Following Guccione and co-workers (Guccione et al., 1991), we assume cardiac tissue to have a preferential axial orientation, defined by the normal unitary vector  $\mathbf{N}_1$ , and a plane orthogonal to this direction, defined by in-plane unitary vectors  $\mathbf{N}_2, \mathbf{N}_3$ . Further, we consider the Green-Lagrange strain tensor components along the local orthonormal basis defined by

$$E_{ij}(\mathbf{F}, \mathbf{N}_i, \mathbf{N}_j) = \mathbf{N}_i \cdot \frac{1}{2} \{ \mathbf{F}^T \mathbf{F} - \mathbf{I} \} \mathbf{N}_j, \quad (2.38)$$

where  $\mathbf{I}$  is the identity tensor. Then, the strain energy density takes the form

$$W(\mathbf{F}) = \frac{c}{2} \{ \exp(Q(\mathbf{F})) - 1 \}, \quad (2.39)$$

where

$$Q(\mathbf{F}) = b_f E_{11}^2 + b_t \{ E_{22}^2 + E_{33}^2 + E_{23}^2 + E_{32}^2 \} + b_{fs} \{ E_{12}^2 + E_{21}^2 + E_{13}^2 + E_{31}^2 \}, \quad (2.40)$$

with  $c, b_f, b_t, b_{fs}$  material parameters for the model. To construct the ETVF form for this case, we set

$$f(\mathbf{F}) = \exp(Q(\mathbf{F})), \quad (2.41)$$

and define the auxiliary variable  $\eta$  implicitly

$$\eta^2 = f(\mathbf{F}) = \exp(Q(\mathbf{F})), \quad (2.42)$$

and constant  $\alpha = 1$ . Further, we take the bijective transformation function  $g(x) = \ln(x)$ , so that

$$g(\eta^2) = 2 \ln(\eta), \quad (2.43)$$

$$g(f(\mathbf{F})) = Q(\mathbf{F}). \quad (2.44)$$

Then, the Lagrangian for this particular constitutive model in the quasi-incompressible case takes the form

$$\begin{aligned} \tilde{Q}[\mathbf{v}, q, \omega, \eta, \xi] = & \int_{\Omega_0} \left\{ \frac{c}{2} \{ \eta^2 - 1 \} - \{ 2 \ln(\eta) - Q(\det(\nabla_0 \mathbf{v})^{-1/3} \nabla_0 \mathbf{v}) \} \xi + \frac{\kappa}{2} \{ \omega - 1 \}^2 - q \{ \det(\nabla_0 \mathbf{v}) - \omega \} \right\} \\ & - \int_{\Omega_0} \mathbf{v} \cdot \mathbf{B} - \int_{\partial \Omega_0^N} \mathbf{v} \cdot \bar{\mathbf{T}}, \quad (2.45) \end{aligned}$$

and the weak form from stationary conditions read: Find  $\boldsymbol{\varphi} \in \mathcal{S}_0$ ,  $p \in \mathcal{P}_0$ ,  $\theta \in \mathcal{P}_0$ ,  $\phi \in \mathcal{P}_0^m$  and  $\boldsymbol{\lambda} \in \mathcal{P}_0^m$  such that

$$D_{\mathbf{v}} \tilde{Q}[\boldsymbol{\varphi}, p, \theta, \phi, \boldsymbol{\lambda}] = \int_{\Omega_0} \hat{P}(\nabla_0 \boldsymbol{\varphi}, \boldsymbol{\lambda}, p) : \nabla_0 \mathbf{v} - \int_{\Omega_0} \mathbf{v} \cdot \mathbf{B} - \int_{\partial\Omega_0^N} \mathbf{v} \cdot \bar{\mathbf{T}} = 0 \quad \forall \mathbf{v} \in \mathcal{V}_0, \quad (2.46)$$

$$D_q \tilde{Q}[\boldsymbol{\varphi}, p, \theta, \phi, \boldsymbol{\lambda}] = \int_{\Omega_0} \{\det(\nabla_0 \boldsymbol{\varphi}) - \theta\} q = 0 \quad \forall q \in \mathcal{P}_0, \quad (2.47)$$

$$D_\omega \tilde{Q}[\boldsymbol{\varphi}, p, \theta, \phi, \boldsymbol{\lambda}] = \int_{\Omega_0} \{\kappa \{\theta - 1\} - p\} \omega = 0 \quad \forall \omega \in \mathcal{P}_0, \quad (2.48)$$

$$D_\eta \tilde{Q}[\boldsymbol{\varphi}, p, \theta, \phi, \boldsymbol{\lambda}] = \int_{\Omega_0} \left\{ c\phi - \frac{2}{\phi} \boldsymbol{\lambda} \right\} \eta = 0 \quad \forall \eta \in \mathcal{P}_0^m, \quad (2.49)$$

$$D_\xi \tilde{Q}[\boldsymbol{\varphi}, p, \theta, \phi, \boldsymbol{\lambda}] = \int_{\Omega_0} \{2 \ln(\phi) - Q(\det(\nabla_0 \boldsymbol{\varphi})^{-1/3} \nabla_0 \boldsymbol{\varphi})\} \xi = 0 \quad \forall \xi \in \mathcal{P}_0^m, \quad (2.50)$$

where  $\hat{P}(\nabla_0 \boldsymbol{\varphi}, \boldsymbol{\lambda}, p)$  takes the form

$$\hat{P}(\mathbf{F}, \boldsymbol{\lambda}, p) = \left\{ \frac{\partial Q}{\partial \mathbf{F}}(\det(\mathbf{F})^{-1/3} \mathbf{F}) \cdot \det(\mathbf{F})^{-1/3} \left\{ -\frac{1}{3} \mathbf{F}^{-T} + \mathbf{I} \right\} \boldsymbol{\lambda} - p \det(\mathbf{F})(\mathbf{F})^{-T} \right\}. \quad (2.51)$$

Similarly, the use of a fully-incompressible approach leads us to the following Lagrangian expression for this particular material

$$\begin{aligned} \tilde{I}[\mathbf{v}, q, \eta, \xi] = & \int_{\Omega_0} \left\{ \frac{c}{2} \{\eta^2 - 1\} - \{2 \ln(\eta) - Q(\nabla_0 \mathbf{v})\} \xi \right\} \\ & - \int_{\Omega_0} q \{\det(\nabla_0 \mathbf{v}) - 1\} - \int_{\Omega_0} \mathbf{v} \cdot \mathbf{B} - \int_{\partial\Omega_0^N} \mathbf{v} \cdot \bar{\mathbf{T}}, \quad (2.52) \end{aligned}$$

and consequently, the weak form from stationary conditions read: Find  $\boldsymbol{\varphi} \in \mathcal{S}_0$ ,  $p \in \mathcal{P}_0$ ,  $\phi \in \mathcal{P}_0^m$  and  $\boldsymbol{\lambda} \in \mathcal{P}_0^m$  such that

$$D_{\mathbf{v}} \tilde{I}[\boldsymbol{\varphi}, p, \phi, \boldsymbol{\lambda}] = \int_{\Omega_0} \tilde{P}(\nabla_0 \boldsymbol{\varphi}, \boldsymbol{\lambda}, p) : \nabla_0 \mathbf{v} - \int_{\Omega_0} \mathbf{v} \cdot \mathbf{B} - \int_{\partial\Omega_0^N} \mathbf{v} \cdot \bar{\mathbf{T}} = 0 \quad \forall \mathbf{v} \in \mathcal{V}_0, \quad (2.53)$$

$$D_q \tilde{I}[\boldsymbol{\varphi}, p, \phi, \boldsymbol{\lambda}] = \int_{\Omega_0} \{\det(\nabla_0 \boldsymbol{\varphi}) - 1\} q = 0 \quad \forall q \in \mathcal{P}_0, \quad (2.54)$$

$$D_\eta \tilde{I}[\boldsymbol{\varphi}, p, \phi, \boldsymbol{\lambda}] = \int_{\Omega_0} \left\{ c\phi - \frac{2}{\phi} \right\} \eta = 0 \quad \forall \eta \in \mathcal{P}_0^m, \quad (2.55)$$

$$D_\xi \tilde{I}[\boldsymbol{\varphi}, p, \phi, \boldsymbol{\lambda}] = \int_{\Omega_0} \{2 \ln(\phi) - Q(\nabla_0 \boldsymbol{\varphi})\} \xi = 0 \quad \forall \xi \in \mathcal{P}_0^m, \quad (2.56)$$

where  $\tilde{P}(\nabla_0 \boldsymbol{\varphi}, \boldsymbol{\lambda}, p)$  takes the form

$$\tilde{P}(\mathbf{F}, \boldsymbol{\lambda}, p) = \left\{ \frac{\partial Q}{\partial \mathbf{F}}(\mathbf{F}) \boldsymbol{\lambda} - p \det(\mathbf{F}) \mathbf{F}^{-T} \right\}. \quad (2.57)$$

### 2.2.2.2. ETVF for a multi-layer model for arterial walls

Here we consider the constitutive model presented by Holzapfel and co-workers (Holzapfel et al., 2000), which has been extensively used in modeling the mechanical behavior of arteries. The model consider the square of the stretch along the collagenous fiber directions, which are represented by unit vectors in the reference configuration  $\mathbf{a}_{0i}$ ,  $i = 1, 2$

$$I_4(\mathbf{F}) := \mathbf{a}_{01} \cdot \mathbf{F}^T \mathbf{F} \mathbf{a}_{01}, \quad (2.58)$$

$$I_6(\mathbf{F}) := \mathbf{a}_{02} \cdot \mathbf{F}^T \mathbf{F} \mathbf{a}_{02}. \quad (2.59)$$

The strain energy density for this model reads

$$W(\mathbf{F}) = \frac{c_1}{2} \{I_1(\mathbf{F}) - 3\} + \sum_{i=4,6} \frac{k_1}{2k_2} \{\exp(k_2 \{I_i(\mathbf{F}) - 1\}^2) - 1\}, \quad (2.60)$$

where  $c_1, k_1, k_2$  are material constants. Then, we define

$$f_i(\mathbf{F}) = \exp(k_2 \{I_i(\mathbf{F}) - 1\}^2) \quad i = 4, 6. \quad (2.61)$$

At the same time, we take  $\alpha_i = 1$  for  $i = 4, 6$ , and define the auxiliary variables  $\eta_i$  implicitly

$$\eta_i^2 = f_i(\mathbf{F}) = \exp(k_2 \{I_i(\mathbf{F}) - 1\}^2) \quad i = 4, 6. \quad (2.62)$$

Further, we consider the bijective transformation function  $g_i(x) = \ln(x)$ , so that

$$g_i(\eta_i^2) = 2 \ln(\eta_i) \quad i = 4, 6; \quad (2.63)$$

and

$$g_i(f_i(\mathbf{F})) = k_2 \{I_i(\mathbf{F}) - 1\}^2 \quad i = 4, 6. \quad (2.64)$$

Then, the Lagrangian for this particular constitutive model in the quasi-incompressible case takes the form

$$\begin{aligned} \tilde{Q}[\mathbf{v}, q, \omega, \eta, \xi] = & \int_{\Omega_0} \left\{ \frac{c_1}{2} \{ \bar{I}_1 (\det(\nabla_0 \mathbf{v}))^{-1/3} \nabla_0 \mathbf{v} - 3 \} + \right. \\ & \left. \sum_{i=4,6} \left\{ \frac{k_1}{2k_2} \{ \eta_i^2 - 1 \} - \left\{ 2 \ln(\eta_i) - k_2 \{ \bar{I}_i (\det(\nabla_0 \mathbf{v}))^{-1/3} \nabla_0 \mathbf{v} - 1 \}^2 \right\} \xi_i \right\} \right\} \\ & + \int_{\Omega_0} \left\{ \frac{\kappa}{2} \{ \omega - 1 \}^2 + q \{ \det(\nabla_0 \mathbf{v}) - \omega \} \right\} - \int_{\Omega_0} \mathbf{v} \cdot \mathbf{B} - \int_{\partial \Omega_0^N} \mathbf{v} \cdot \bar{\mathbf{T}}. \quad (2.65) \end{aligned}$$

and the weak form from stationary conditions read: Find  $\boldsymbol{\varphi} \in \mathcal{S}_0$ ,  $p \in \mathcal{P}_0$ ,  $\theta \in \mathcal{P}_0$ ,  $\phi \in \mathcal{P}_0^m$  and  $\boldsymbol{\lambda} \in \mathcal{P}_0^m$  such that

$$D_{\mathbf{v}} \tilde{Q}[\boldsymbol{\varphi}, p, \theta, \phi, \boldsymbol{\lambda}] = \int_{\Omega_0} \hat{P}(\nabla_0 \boldsymbol{\varphi}, \lambda, p) : \nabla_0 \mathbf{v} - \int_{\Omega_0} \mathbf{v} \cdot \mathbf{B} - \int_{\partial\Omega_0^N} \mathbf{v} \cdot \bar{\mathbf{T}} = 0 \quad \forall \mathbf{v} \in \mathcal{V}_0, \quad (2.66)$$

$$D_q \tilde{Q}[\boldsymbol{\varphi}, p, \theta, \phi, \boldsymbol{\lambda}] = \int_{\Omega_0} \{\det(\nabla_0 \boldsymbol{\varphi}) - \theta\} q = 0 \quad \forall q \in \mathcal{P}_0, \quad (2.67)$$

$$D_\omega \tilde{Q}[\boldsymbol{\varphi}, p, \theta, \phi, \boldsymbol{\lambda}] = \int_{\Omega_0} \{\kappa \{\theta - 1\} - p\} \omega = 0 \quad \forall \omega \in \mathcal{P}_0, \quad (2.68)$$

$$D_\eta \tilde{Q}[\boldsymbol{\varphi}, p, \theta, \phi, \boldsymbol{\lambda}] = \int_{\Omega_0} \left\{ c\phi - \frac{2}{\phi} \lambda \right\} \eta = 0 \quad \forall \eta \in \mathcal{P}_0^m, \quad (2.69)$$

$$D_\xi \tilde{Q}[\boldsymbol{\varphi}, p, \theta, \phi, \boldsymbol{\lambda}] = \int_{\Omega_0} \sum_{i=4,6} \left\{ 2 \ln(\phi_i) - k_2 \{ \bar{I}_i(\nabla_0 \boldsymbol{\varphi}) - 1 \}^2 \right\} \xi_i = 0 \quad \forall \xi \in \mathcal{P}_0^m, \quad (2.70)$$

where  $\hat{P}(\nabla_0 \boldsymbol{\varphi}, \lambda, p)$  takes the forms

$$\begin{aligned} \hat{P}(\mathbf{F}, \lambda, p) = & \det(\mathbf{F})^{-1/3} \left\{ -\frac{1}{3} \mathbf{F}^{-T} + \mathbf{I} \right\} \\ & \cdot \left\{ \frac{c_1}{2} \frac{\partial \bar{I}_1}{\partial \mathbf{F}} (\det(\mathbf{F})^{-1/3} \mathbf{F}) + \sum_{i=4,6} 2k_2 \{ \bar{I}_i (\det(\mathbf{F})^{-1/3} \mathbf{F}) - 1 \} \frac{\partial \bar{I}_i}{\partial \mathbf{F}} (\det(\mathbf{F})^{-1/3} \mathbf{F}) \lambda_i \right\} \\ & - p \det(\mathbf{F}) (\mathbf{F})^{-T}. \quad (2.71) \end{aligned}$$

Following the same procedure, we reach a Lagrangian expression in the fully-incompressible case for this particular model

$$\begin{aligned} \tilde{I}[\mathbf{v}, q, \eta, \xi] = & \\ \int_{\Omega_0} \left\{ \frac{c_1}{2} \{I_1(\nabla_0 \mathbf{v}) - 3\} + \sum_{i=4,6} \left\{ \frac{k_1}{2k_2} \{\eta_i^2 - 1\} - \{2 \ln(\eta_i) - k_2 \{I_i(\nabla_0 \mathbf{v}) - 1\}^2\} \xi_i \right\} \right\} & \\ - \int_{\Omega_0} q \{\det(\nabla_0 \mathbf{v}) - 1\} - \int_{\Omega_0} \mathbf{v} \cdot \mathbf{B} - \int_{\partial\Omega_0^N} \mathbf{v} \cdot \bar{\mathbf{T}}, & \quad (2.72) \end{aligned}$$

as a consequence, the weak form reads: Find  $\boldsymbol{\varphi} \in \mathcal{S}_0$ ,  $p \in \mathcal{P}_0$ ,  $\phi \in \mathcal{P}_0^m$  and  $\boldsymbol{\lambda} \in \mathcal{P}_0^m$  such that

$$D_{\mathbf{v}} \tilde{I}[\boldsymbol{\varphi}, p, \phi, \boldsymbol{\lambda}] = \int_{\Omega_0} \tilde{P}(\nabla_0 \boldsymbol{\varphi}, \boldsymbol{\lambda}, p) : \nabla_0 \mathbf{v} - \int_{\Omega_0} \mathbf{v} \cdot \mathbf{B} - \int_{\partial\Omega_0^N} \mathbf{v} \cdot \bar{\mathbf{T}} = 0 \quad \forall \mathbf{v} \in \mathcal{V}_0, \quad (2.73)$$

$$D_q \tilde{I}[\boldsymbol{\varphi}, p, \phi, \boldsymbol{\lambda}] = \int_{\Omega_0} \{\det(\nabla_0 \boldsymbol{\varphi}) - 1\} q = 0 \quad \forall q \in \mathcal{P}_0, \quad (2.74)$$

$$D_\eta \tilde{I}[\boldsymbol{\varphi}, p, \phi, \boldsymbol{\lambda}] = \int_{\Omega_0} \left\{ c\phi - \frac{2}{\phi} \right\} \eta = 0 \quad \forall \eta \in \mathcal{P}_0^m, \quad (2.75)$$

$$D_\xi \tilde{I}[\boldsymbol{\varphi}, p, \phi, \boldsymbol{\lambda}] = \sum_{i=4,6} \int_{\Omega_0} \{2 \ln(\phi_i) - k_2 \{I_i(\nabla_0 \boldsymbol{\varphi}) - 1\}^2\} \xi_i = 0 \quad \forall \xi \in \mathcal{P}_0^m, \quad (2.76)$$

where  $\tilde{P}(\nabla_0 \boldsymbol{\varphi}, \boldsymbol{\lambda}, p)$  takes the form

$$\tilde{P}(\mathbf{F}, \boldsymbol{\lambda}, p) = \frac{c_1}{2} \frac{\partial I_1}{\partial \mathbf{F}}(\mathbf{F}) + \sum_{i=4,6} 2k_2 \{I_i(\mathbf{F}) - 1\} \frac{\partial I_i}{\partial \mathbf{F}}(\mathbf{F}) \boldsymbol{\lambda}_i - p \det(\mathbf{F})(\mathbf{F})^{-T}. \quad (2.77)$$

### 2.2.2.3. ETVF for structurally-based model for passive myocardium

Following Holzapfel and Ogden (Holzapfel & Ogden, 2009), we characterize the orthotropic passive behavior of cardiac tissue by defining a fiber direction  $\mathbf{f}_0$  that indicates the main orientation of cardiac muscle cells within the tissue, and a sheet direction  $\mathbf{s}_0$ , orthogonal to  $\mathbf{f}_0$ , such that both vectors define the sheet plane between bundles of cardiac muscle cells that is mainly composed of collagen fibers. Here, we consider the main invariants

$$I_{4f}(\mathbf{F}) := \mathbf{f}_0 \cdot \mathbf{F}^T \mathbf{F} \mathbf{f}_0, \quad (2.78)$$

$$I_{4s}(\mathbf{F}) := \mathbf{s}_0 \cdot \mathbf{F}^T \mathbf{F} \mathbf{s}_0, \quad (2.79)$$

$$I_{8fs}(\mathbf{F}) := \mathbf{f}_0 \cdot \mathbf{F}^T \mathbf{F} \mathbf{s}_0. \quad (2.80)$$

Then, the strain energy density takes the form

$$W(\mathbf{F}) = \sum_{j=1,4f,4s,8fs} \frac{a_j}{2b_j} \{ \exp(b_j \{I_j(\mathbf{F}) - \beta_j\}^{\gamma_j}) - \alpha_j \}, \quad (2.81)$$

where,  $a_1, b_1, a_f, b_f, a_s, b_s, a_{fs}, b_{fs}$  are material constant. Additionally, the constitutive model for the case of passive myocardium (Holzapfel & Ogden, 2009) assumes that  $\alpha_1 = 3$ ,  $\alpha_{4f} = 1$ ,  $\alpha_{4s} = 1$ , and  $\alpha_{8fs} = 0$ ,  $\beta_1 = 3$ ,  $\beta_{4f} = 1$ ,  $\beta_{4s} = 1$ ,  $\beta_{8fs} = 0$ , and  $\gamma_1 = 1$ ,  $\gamma_{4f} = 2$ ,  $\gamma_{4s} = 2$ ,  $\gamma_{8fs} = 2$ . We set

$$f_i(\mathbf{F}) = \exp(b_i \{I_i(\mathbf{F}) - \beta_i\}^{\gamma_i}) \quad i = 1, 4f, 4s, 8fs. \quad (2.82)$$

and define the auxiliary variables  $\eta_j$  implicitly as

$$\eta_i^2 = f_i(\mathbf{F}) = \exp(b_i \{I_i(\mathbf{F}) - \beta_i\}^{\gamma_i}) \quad i = 1, 4f, 4s, 8fs. \quad (2.83)$$

Further, we take the bijective transformation function  $g_j(x) = \ln(x)$ , so that

$$g_i(\eta_i^2) = 2 \ln(\eta_i) \quad i = 1, 4f, 4s, 8fs. \quad (2.84)$$

Then,

$$g_i(f_i(\mathbf{F})) = b_i \{I_i(\mathbf{F}) - \beta_i\}^{\gamma_i} \quad i = 1, 4f, 4s, 8fs. \quad (2.85)$$

Consequently, the Lagrangian for this particular constitutive model in the quasi-incompressible case takes the form

$$\begin{aligned} \tilde{Q}[\mathbf{v}, q, \omega, \eta, \xi] = & \\ & \int_{\Omega_0} \left\{ \sum_{i=1,4f,4s,8fs} \frac{a_i}{2b_i} \{\eta_i^2 - \alpha_i\} - \{2 \ln(\eta_i) - b_i \{\bar{I}_i(\det(\nabla_0 \mathbf{v})^{-1/3} \nabla_0 \mathbf{v}) - \beta_i\}^{\gamma_i}\} \xi_i \right\} \\ & - \int_{\Omega_0} \left\{ \frac{\kappa}{2} \{\omega - 1\}^2 + q \{\det(\nabla_0 \mathbf{v}) - \omega\} \right\} - \int_{\Omega_0} \mathbf{v} \cdot \mathbf{B} - \int_{\partial\Omega_0^N} \mathbf{v} \cdot \bar{\mathbf{T}}. \end{aligned} \quad (2.86)$$

and the weak form from stationary conditions read: Find  $\varphi \in \mathcal{S}_0$ ,  $p \in \mathcal{P}_0$ ,  $\theta \in \mathcal{P}_0$ ,  $\phi \in \mathcal{P}_0^m$  and  $\lambda \in \mathcal{P}_0^m$  such that

$$D_{\mathbf{v}} \tilde{Q}[\varphi, p, \theta, \phi, \lambda] = \int_{\Omega_0} \hat{P}(\nabla_0 \varphi, \lambda, p) : \nabla_0 \mathbf{v} - \int_{\Omega_0} \mathbf{v} \cdot \mathbf{B} - \int_{\partial\Omega_0^N} \mathbf{v} \cdot \bar{\mathbf{T}} = 0 \quad \forall \mathbf{v} \in \mathcal{V}_0, \quad (2.87)$$

$$D_q \tilde{Q}[\varphi, p, \theta, \phi, \lambda] = \int_{\Omega_0} \{\det(\nabla_0 \varphi) - \theta\} q = 0 \quad \forall q \in \mathcal{P}_0, \quad (2.88)$$

$$D_\omega \tilde{Q}[\varphi, p, \theta, \phi, \lambda] = \int_{\Omega_0} \{\kappa \{\theta - 1\} - p\} \omega = 0 \quad \forall \omega \in \mathcal{P}_0, \quad (2.89)$$

$$D_\eta \tilde{Q}[\varphi, p, \theta, \phi, \lambda] = \int_{\Omega_0} \sum_{i=1,4f,4s,8fs} \left\{ \frac{a_i}{b_i} \phi_i - \frac{2}{\phi_i} \right\} \eta_i = 0 \quad \forall \eta \in \mathcal{P}_0^m, \quad (2.90)$$

$$D_\xi \tilde{Q}[\varphi, p, \theta, \phi, \lambda] = \int_{\Omega_0} \sum_{i=1,4f,4s,8fs} \{2 \ln(\phi_i) - b_i \{\bar{I}_i(\nabla_0 \varphi) - \beta_i\}^{\gamma_i}\} \xi_i = 0 \quad \forall \xi \in \mathcal{P}_0^m, \quad (2.91)$$

where  $\hat{P}(\nabla_0 \boldsymbol{\varphi}, \lambda, p)$  takes the forms

$$\begin{aligned} \hat{P}(\mathbf{F}, \lambda, p) = & \sum_{i=1,4f,4s,8fs} \gamma_i b_i \left\{ \bar{I}_i (\det(\mathbf{F})^{-1/3} \mathbf{F}) - \beta_i \right\}^{\gamma_i - 1} \frac{\partial \bar{I}_i}{\partial \mathbf{F}} (\det(\mathbf{F})^{-1/3} \mathbf{F}) \\ & \cdot \det(\mathbf{F})^{-1/3} \left\{ -\frac{1}{3} \mathbf{F}^{-T} + \mathbf{I} \right\} \lambda_i - p \det(\mathbf{F}) (\mathbf{F})^{-T}. \end{aligned} \quad (2.92)$$

For the fully-incompressible formulation, the Lagrangian in this case reads

$$\begin{aligned} \tilde{I}[\mathbf{v}, q, \eta, \xi] = & \int_{\Omega_0} \sum_{i=1,4f,4s,8fs} \left\{ \frac{a_i}{2b_i} \{ \eta_i^2 - \alpha_i \} - \{ 2 \ln(\eta_i) - b_i \{ I_i(\nabla_0 \mathbf{v}) - \beta_i \}^{\gamma_i} \} \xi_i \right\} \\ & - \int_{\Omega_0} q \{ \det(\nabla_0 \mathbf{v}) - 1 \} - \int_{\Omega_0} \mathbf{v} \cdot \mathbf{B} - \int_{\partial \Omega_0^N} \mathbf{v} \cdot \bar{\mathbf{T}}. \end{aligned} \quad (2.93)$$

and the weak form from stationary conditions read: Find  $\boldsymbol{\varphi} \in \mathcal{S}_0$ ,  $p \in \mathcal{P}_0$ ,  $\phi \in \mathcal{P}_0^m$  and  $\boldsymbol{\lambda} \in \mathcal{P}_0^m$  such that

$$D_{\mathbf{v}} \tilde{I}[\boldsymbol{\varphi}, p, \phi, \boldsymbol{\lambda}] = \int_{\Omega_0} \tilde{P}(\nabla_0 \boldsymbol{\varphi}, \lambda, p) : \nabla_0 \mathbf{v} - \int_{\Omega_0} \mathbf{v} \cdot \mathbf{B} - \int_{\partial \Omega_0^N} \mathbf{v} \cdot \bar{\mathbf{T}} = 0 \quad \forall \mathbf{v} \in \mathcal{V}_0, \quad (2.94)$$

$$D_q \tilde{I}[\boldsymbol{\varphi}, p, \phi, \boldsymbol{\lambda}] = \int_{\Omega_0} \{ \det(\nabla_0 \boldsymbol{\varphi}) - 1 \} q = 0 \quad \forall q \in \mathcal{P}_0, \quad (2.95)$$

$$D_\eta \tilde{I}[\boldsymbol{\varphi}, p, \phi, \boldsymbol{\lambda}] = \int_{\Omega_0} \sum_{i=1,4f,4s,8fs} \left\{ \frac{a_i}{b_i} \phi_i - \frac{2}{\phi_i} \right\} \eta_i = 0 \quad \forall \eta \in \mathcal{P}_0^m, \quad (2.96)$$

$$D_\xi \tilde{I}[\boldsymbol{\varphi}, p, \phi, \boldsymbol{\lambda}] = \int_{\Omega_0} \sum_{i=1,4f,4s,8fs} \{ 2 \ln(\phi_i) - b_i \{ I_i(\nabla_0 \boldsymbol{\varphi}) - \beta_i \}^{\gamma_i} \} \xi_i = 0 \quad \forall \xi \in \mathcal{P}_0^m, \quad (2.97)$$

where  $\tilde{P}(\nabla_0\varphi, \lambda, p)$  is defined as

$$\tilde{P}(\mathbf{F}, \lambda, p) = \sum_{i=1,4f,4s,8fs} \gamma_i b_i \{I_i(\mathbf{F}) - \beta_i\}^{\gamma_i-1} \frac{\partial I_i}{\partial \mathbf{F}}(\mathbf{F}) \lambda_i - p \det(\mathbf{F})(\mathbf{F})^{-T}. \quad (2.98)$$

### 2.2.3. Linearization of the weak form

The solution of the nonlinear problems resulting from the ETVF can be approached by means of linearization. To this end, we express the set of weak equations of the quasi-incompressible formulation as a multi-field problem of the form: Find  $\chi \in S_0$  such that

$$G[\chi, \Theta] = \mathbf{0} \quad \forall \Theta \in V_0, \quad (2.99)$$

where  $\chi = [\varphi, p, \theta, \phi, \lambda]$  is a multi-field vector in the space  $S_0 = \mathcal{V}_0 \times \mathcal{P}_0 \times \mathcal{P}_0 \times \mathcal{P}_0^m \times \mathcal{P}_0^m$ , and  $[\mathbf{v}, q, \omega, \eta, \xi]$  is a multi-field test function in the space  $V_0 = \mathcal{V}_0 \times \mathcal{P}_0 \times \mathcal{P}_0 \times \mathcal{P}_0^m \times \mathcal{P}_0^m$ , and the residual reads

$$G[\chi, \Theta] = \begin{bmatrix} D_{\mathbf{v}} \tilde{Q}[\chi] \\ D_q \tilde{Q}[\chi] \\ D_\omega \tilde{Q}[\chi] \\ D_\eta \tilde{Q}[\chi] \\ D_\xi \tilde{Q}[\chi] \end{bmatrix}. \quad (2.100)$$

Then, to solve (2.99), we linearize around an initial guess  $\chi \in S_0$  and solve the linear problem: Find the increment  $\Delta\chi \in V_0$  such that

$$G[\chi, \Theta] + TG[\chi, \Theta]\Delta\chi = \mathbf{0} \quad \forall \Theta \in V_0, \quad (2.101)$$

where the tangent operator  $TG$  takes the form

$$TG[\boldsymbol{\chi}, \boldsymbol{\Theta}] = \begin{bmatrix} D_{\mathbf{v}, \Delta \varphi}^2 \tilde{Q}[\boldsymbol{\chi}] & D_{\mathbf{v}, \Delta p}^2 \tilde{Q}[\boldsymbol{\chi}] & D_{\mathbf{v}, \Delta \theta}^2 \tilde{Q}[\boldsymbol{\chi}] & D_{\mathbf{v}, \Delta \phi}^2 \tilde{Q}[\boldsymbol{\chi}] & D_{\mathbf{v}, \Delta \lambda}^2 \tilde{Q}[\boldsymbol{\chi}] \\ D_{q, \Delta \varphi}^2 \tilde{Q}[\boldsymbol{\chi}] & D_{q, \Delta p}^2 \tilde{Q}[\boldsymbol{\chi}] & D_{q, \Delta \theta}^2 \tilde{Q}[\boldsymbol{\chi}] & D_{q, \Delta \phi}^2 \tilde{Q}[\boldsymbol{\chi}^h] & D_{q, \Delta \lambda}^2 \tilde{Q}[\boldsymbol{\chi}^h] \\ D_{\omega, \Delta \varphi}^2 \tilde{Q}[\boldsymbol{\chi}] & D_{\omega, \Delta p}^2 \tilde{Q}[\boldsymbol{\chi}] & D_{\omega, \Delta \theta}^2 \tilde{Q}[\boldsymbol{\chi}] & D_{\omega, \Delta \phi}^2 \tilde{Q}[\boldsymbol{\chi}] & D_{\omega, \Delta \lambda}^2 \tilde{Q}[\boldsymbol{\chi}] \\ D_{\boldsymbol{\eta}, \Delta \varphi}^2 \tilde{Q}[\boldsymbol{\chi}] & D_{\boldsymbol{\eta}, \Delta p}^2 \tilde{Q}[\boldsymbol{\chi}] & D_{\boldsymbol{\eta}, \Delta \theta}^2 \tilde{Q}[\boldsymbol{\chi}] & D_{\boldsymbol{\eta}, \Delta \phi}^2 \tilde{Q}[\boldsymbol{\chi}] & D_{\boldsymbol{\eta}, \Delta \lambda}^2 \tilde{Q}[\boldsymbol{\chi}] \\ D_{\boldsymbol{\xi}, \Delta \varphi}^2 \tilde{Q}[\boldsymbol{\chi}] & D_{\boldsymbol{\xi}, \Delta p}^2 \tilde{Q}[\boldsymbol{\chi}] & D_{\boldsymbol{\xi}, \Delta \theta}^2 \tilde{Q}[\boldsymbol{\chi}] & D_{\boldsymbol{\xi}, \Delta \phi}^2 \tilde{Q}[\boldsymbol{\chi}] & D_{\boldsymbol{\xi}, \Delta \lambda}^2 \tilde{Q}[\boldsymbol{\chi}] \end{bmatrix}. \quad (2.102)$$

The case of fully-incompressible formulations can be approached in a similar manner. We start by considering the multi-field problem: Find  $\boldsymbol{\chi} \in S_0$  such that

$$H[\boldsymbol{\chi}, \boldsymbol{\Theta}] = \mathbf{0} \quad \forall \boldsymbol{\Theta} \in V_0. \quad (2.103)$$

Here, we consider  $\boldsymbol{\chi} = [\varphi, p, \phi, \boldsymbol{\lambda}]$  as a multi-field vector in the space  $S_0 = \mathcal{V}_0 \times \mathcal{P}_0 \times \mathcal{P}_0^m \times \mathcal{P}_0^m$ , and  $[\mathbf{v}, q, \boldsymbol{\eta}, \boldsymbol{\xi}]$  as the multi-field test function in the space  $V_0 = \mathcal{V}_0 \times \mathcal{P}_0 \times \mathcal{P}_0^m \times \mathcal{P}_0^m$ . Then, the linearization is analogous to that developed above, which lead us to following problem: Find the increment  $\Delta \boldsymbol{\chi} \in V_0$  such that

$$H[\boldsymbol{\chi}, \boldsymbol{\Theta}] + TH[\boldsymbol{\chi}, \boldsymbol{\Theta}] \Delta \boldsymbol{\chi} = \mathbf{0} \quad \forall \boldsymbol{\Theta} \in V_0, \quad (2.104)$$

where the residual is written as

$$G[\boldsymbol{\chi}, \boldsymbol{\Theta}] = \begin{bmatrix} D_{\mathbf{v}} \tilde{Q}[\boldsymbol{\chi}] \\ D_q \tilde{Q}[\boldsymbol{\chi}] \\ D_{\boldsymbol{\eta}} \tilde{Q}[\boldsymbol{\chi}] \\ D_{\boldsymbol{\xi}} \tilde{Q}[\boldsymbol{\chi}] \end{bmatrix}, \quad (2.105)$$

and the tangent operator  $TH$  reads

$$TH[\boldsymbol{\chi}, \Theta] = \begin{bmatrix} D_{\mathbf{v}, \Delta \varphi}^2 \tilde{I}[\boldsymbol{\chi}] & D_{\mathbf{v}, \Delta p}^2 \tilde{I}[\boldsymbol{\chi}] & D_{\mathbf{v}, \Delta \phi}^2 \tilde{I}[\boldsymbol{\chi}] & D_{\mathbf{v}, \Delta \lambda}^2 \tilde{I}[\boldsymbol{\chi}] \\ D_{q, \Delta \varphi}^2 \tilde{I}[\boldsymbol{\chi}] & D_{q, \Delta p}^2 \tilde{I}[\boldsymbol{\chi}] & D_{q, \Delta \phi}^2 \tilde{I}[\boldsymbol{\chi}] & D_{q, \Delta \lambda}^2 \tilde{I}[\boldsymbol{\chi}] \\ D_{\boldsymbol{\eta}, \Delta \varphi}^2 \tilde{I}[\boldsymbol{\chi}] & D_{\boldsymbol{\eta}, \Delta p}^2 \tilde{I}[\boldsymbol{\chi}] & D_{\boldsymbol{\eta}, \Delta \phi}^2 \tilde{I}[\boldsymbol{\chi}] & D_{\boldsymbol{\eta}, \Delta \lambda}^2 \tilde{I}[\boldsymbol{\chi}] \\ D_{\boldsymbol{\xi}, \Delta \varphi}^2 \tilde{I}[\boldsymbol{\chi}] & D_{\boldsymbol{\xi}, \Delta p}^2 \tilde{I}[\boldsymbol{\chi}] & D_{\boldsymbol{\xi}, \Delta \phi}^2 \tilde{I}[\boldsymbol{\chi}] & D_{\boldsymbol{\xi}, \Delta \lambda}^2 \tilde{I}[\boldsymbol{\chi}] \end{bmatrix}. \quad (2.106)$$

The expressions for the entries of the tangent operators defined in (2.102) and (2.106) are included in Appendix A.

#### 2.2.4. Multi-field finite-element discretization and solution

We use a finite-element scheme to discretize the infinite-dimensional linearized problem stated in (2.101) and (2.104). To this end, let  $\Omega_0^h = \cup_{e=1}^{N_{el}} \Omega_e$  be a domain discretization where  $N_{el}$  is the number of elements, and all elements satisfy the condition  $\Omega_i \cap \Omega_j = \emptyset$  for  $i \neq j$ . Based on such discretization, we introduce the finite-dimensional subspaces

$$\mathcal{V}_0^h := \{v^h : \Omega_0^h \rightarrow \mathbb{R}^d \text{ such that } v^h(X) = \sum_{A=1}^{N_{dofs}} N_A(X) v_A\} \subset \mathcal{V}_0, \quad (2.107)$$

$$\mathcal{P}_0^h := \{q^h : \Omega_0^h \rightarrow \mathbb{R}^d \text{ such that } q^h(X) = \sum_{A=1}^{N_{dofs}} N_A(X) q_A\} \subset \mathcal{P}_0, \quad (2.108)$$

$$\mathcal{P}_0^{m,h} := \{\eta^h : \Omega_0^h \rightarrow \mathbb{R}^d \text{ such that } \eta^h(X) = \sum_{A=1}^{N_{dofs}} N_A(X) \eta_A\} \subset \mathcal{P}_0^m. \quad (2.109)$$

In the preceding definitions,  $\{N_A\}_{a=1}^{N_{dofs}}$  are the basis functions,  $N_{dofs}$  is the number of element nodes with unknown degrees of freedom, and  $v_A$ ,  $q_A$ , and  $\boldsymbol{\eta}_A$  are the nodal coefficients for each field. We use the same element basis functions to set the trial space

$$\mathcal{S}_0^h := \{\varphi^h : \Omega_0^h \rightarrow \mathbb{R}^d \text{ such that } \varphi^h(X) = \sum_{A=1}^{N_{dofs}} N_A(X) \varphi_A + \bar{\varphi}(X)\} \subset \mathcal{S}_0, \quad (2.110)$$

where  $\varphi_A$  correspond to the nodal values of the displacement field, and  $\bar{\varphi}(X)$  is a function that satisfies the boundary conditions in (2.3). Considering the FE spaces defined above, we evaluate the linearized problem (2.101) in  $\chi^h = [\varphi^h, p^h, \theta^h, \phi^h, \lambda^h]$ , which is a multi-field vector in the space  $S_0^h = \mathcal{V}_0^h \times \mathcal{P}_0^h \times \mathcal{P}_0^h \times \mathcal{P}_0^{m,h} \times \mathcal{P}_0^{m,h}$ . As a consequence, we reach a FE problem for the quasi-incompressible formulation that reads: Find the increment  $\Delta\chi^h \in V_0^h$  such that:

$$G[\chi^h, \Theta^h] + TG[\chi^h, \Theta^h]\Delta\chi^h = \mathbf{0} \quad \forall \Theta^h \in V_0^h, \quad (2.111)$$

For the fully-incompressible formulation, the procedure is analogous to that developed above, but here we consider  $\chi^h = [\varphi^h, p^h, \theta^h, \phi^h, \lambda^h]$ , which lead us to the linearized FE problem that reads: Find  $\Delta\chi^h \in V_0^h$  such that

$$H[\chi^h, \Theta^h] + TH[\chi^h, \Theta^h]\Delta\chi^h = \mathbf{0} \quad \forall \Theta^h \in V_0^h. \quad (2.112)$$

### 2.3. Numerical simulations

In the following, we report on the simulation of three examples of cardiovascular problems of interest to compare the accuracy and the numerical performance of the ETVF method against standard variational formulations (Standard FE) summarized in 2.2.1. To this end, we implemented the ETVF for the full-incompressible and quasi-incompressible cases using different interpolation schemes using the library FEniCS (Logg, Mardal, Wells, et al., 2012). The Python codes are available for download at <https://github.com/dehurtado/ETVF>. All simulations were performed on a workstation with Intel(R) Core(TM) i7-7700HQ CPU @2.8GHz processor, running on a single core. We employed a Newton-Raphson scheme to solve the resulting non-linear problems, always using a preconditioned Krylov's solver (GMRES-ILU) for the solution of the linear systems arising at each Newton iteration (Saad & Schultz, 1986). We used a tolerance of 1E-6 for both Newton and GMRES-ILU solvers. Figure 2.1 show schematics of the geometries and loading conditions considered in the three simulations studied in

this work. Table 2.2 summarizes the constitutive models and parameter values employed in each simulation.

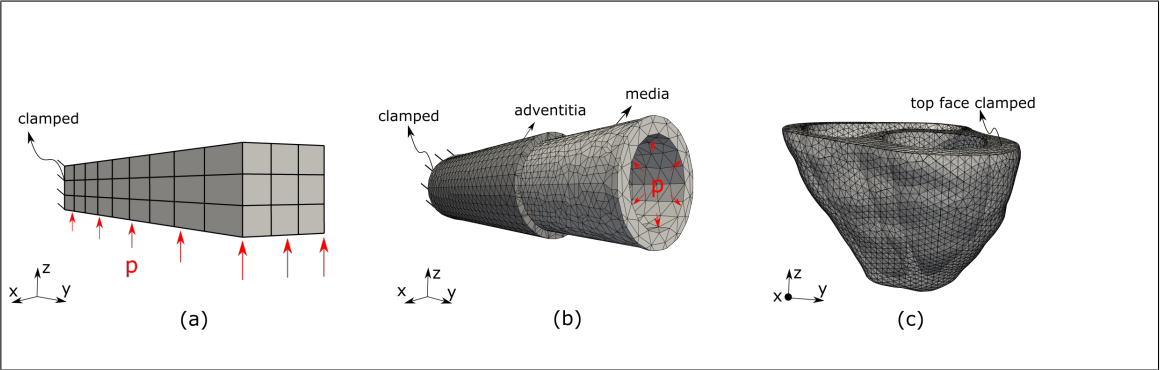


Figure 2.1. Geometry and loading of three examples of cardiovascular simulations: (a) Cardiac beam benchmark (mesh with 208 nodes and 648 elements), (b) Artery inflation (mesh with 1,661 nodes and 4,896 elements), (c) Biventricular chambers under passive filling (mesh with 8,612 nodes and 37,127 elements).

Simulation	Model	Strain energy density function	Parameters
Cardiac beam benchmark	Guccione et al. [10, 21]	$W[\varphi] = \frac{c}{2} (\exp\{Q\} - 1)$ , where $Q = b_f E_{11}^2 + b_t (E_{22}^2 + E_{33}^2 + E_{23}^2 + E_{32}^2) + b_{fs} (E_{12}^2 + E_{21}^2 + E_{13}^2 + E_{31}^2)$ E : Green - Lagrange strain tensor change of variable: $g(\eta^2) = 2 \ln(\eta)$	$c = 2.0[\text{kPa}] ; b_f = 8.0[-]$ $b_t = 2.0[-] ; b_{fs} = 4.0[-]$
Artery Inflation	Holzapfel et al. - vessels [12]	$W[\varphi] = \frac{c_1}{2} (I_1 - 3)$ $+ \sum_{4,6} \frac{k_1}{2k_2} (\exp\{k_2 (I_i - 1)^2\} - 1)$ change of variable: $g(\eta^2) = 2 \ln(\eta)$	$c_{1M} = 3.0[\text{kPa}] ; c_{1A} = 0.3[\text{kPa}]$ $k_{1M} = 2.36[\text{kPa}] ; k_{1A} = 0.56[\text{kPa}]$ $k_{2M} = 0.84[-] ; k_{2A} = 0.71[-]$ M : media ; A : adventitia
Passive filing of biventricular chambers	Holzapfel et al. - cardiac [13, 7, 9]	$W[\varphi] = \frac{a_1}{2b_1} \exp\{b_1 (I_1 - 3)\}$ $+ \sum_{4f,4s} \frac{a_j}{2b_j} (\exp\{b_j (I_j - 1)^2\} - 1)$ $+ \frac{a_{fs}}{2b_{fs}} (\exp\{b_{fs} I_{8fs}^2\} - 1)$ change of variable: $g(\eta^2) = 2 \ln(\eta)$	$a_1 = 0.24[\text{kPa}] ; b_1 = 5.08[-]$ $a_{4f} = 1.46[\text{kPa}] ; b_{4f} = 4.15[-]$ $a_{4s} = 0.87[\text{kPa}] ; b_{4s} = 1.6[-]$ $a_{8fs} = 0.3[\text{kPa}] ; b_{8fs} = 1.3[-]$ <i>f</i> : fiber ; <i>s</i> : sheet

Figure 2.2. Constitutive models and parameter values for the simulations considered in this study.

### 2.3.1. Cardiac beam benchmark

Following a benchmark study on cardiac mechanics models reported in the literature (Land et al., 2015), we considered the case of a cardiac beam with domain  $[0, 10] \times [0, 1] \times [0, 1] \text{ mm}^3$ . Figure 2.1(a) shows a representation of the geometry, loads, and boundary conditions (beam is fully clamped at  $x=0$ ), along with the FE discretization employed. A constant pressure of 0.004 kPa was applied on the bottom surface of the beam, and the beam assumed the transversely isotropic constitutive law presented in Section 2.2.2.1 with fibers oriented along the axial direction  $(1, 0, 0)$ . The domain was

discretized using regular hexahedral elements, with different degrees of interpolation for the unknown fields. We considered as a baseline the results reported by the PUC-FEAP team in a previous benchmark study (Land et al., 2015), which were obtained using a  $Q_1 - P_0$  quasi-incompressible formulation. In our simulations, we employed  $Q_2 - Q_1$  and  $Q_2 - P_0$  elements for the fully-incompressible case and  $Q_2 - Q_1$  and  $Q_1 - P_0$  for the quasi-incompressible case.

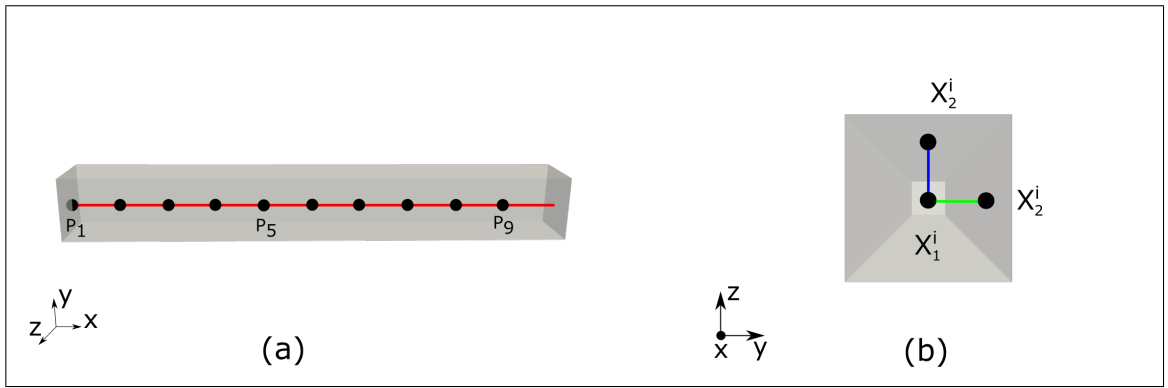


Figure 2.3. Cardiac beam benchmark. (a) Points along the beam axis where strain was reported, (b) Local axis for the beam cross-section. Based on Land et al. (2015).

Since no analytical solutions exist to this benchmark problem, we assessed the accuracy and performance of the ETVF models by comparing their results to those predicted by the Standard FE simulations. Following the benchmark study (Land et al., 2015), we computed strains along the x,y and z axes using a finite differences scheme, and tracked the changes in distance between the reference ( $X_i$ ) and actual ( $x_i$ ) states for the lines formed by the x-spaced points, see Figure 2.3. Strain values were computed as

$$S_i = \left( \frac{\|x_1^i - x_2^i\|}{\|X_1^i - X_2^i\|} - 1 \right), \quad i = 0, 1, \dots, n. \quad (2.113)$$

To be consistent with the literature, we calculate the strains along the line  $(x, 0.5, 0.5)$  for the x-direction, using  $X_1^i = (i, 0.5, 0.5)$  and  $X_2^i = (i + 1, 0.5, 0.5)$  with  $i = 1, \dots, 8$ . At the same time, for transverse strain we use  $X_1^i = (i, 0.5, 0.5)$  and  $X_2^i = (i, 0.9, 0.5)$  for y-direction, and  $X_1^i = (i, 0.5, 0.5)$  and  $X_2^i = (i, 0.5, 0.9)$  for z-direction with  $i = 1, \dots, 9$  for both.

Figure 2.4 and Figure 2.5 report the strain values predicted by the Standard FE and ETVF models in the quasi-incompressible and fully-incompressible cases, respectively. These figures also include the results reported in the literature (Land et al., 2015). The strains predicted by both formulations under different interpolation schemes coincide in all cases, and closely follow the results by the PUC-FEAP team in the benchmark study. For the fully-incompressible case, all simulations delivered highly consistent results for the strains along y and z-axis in comparison with baseline, see Figures 2.5(b) and (c).

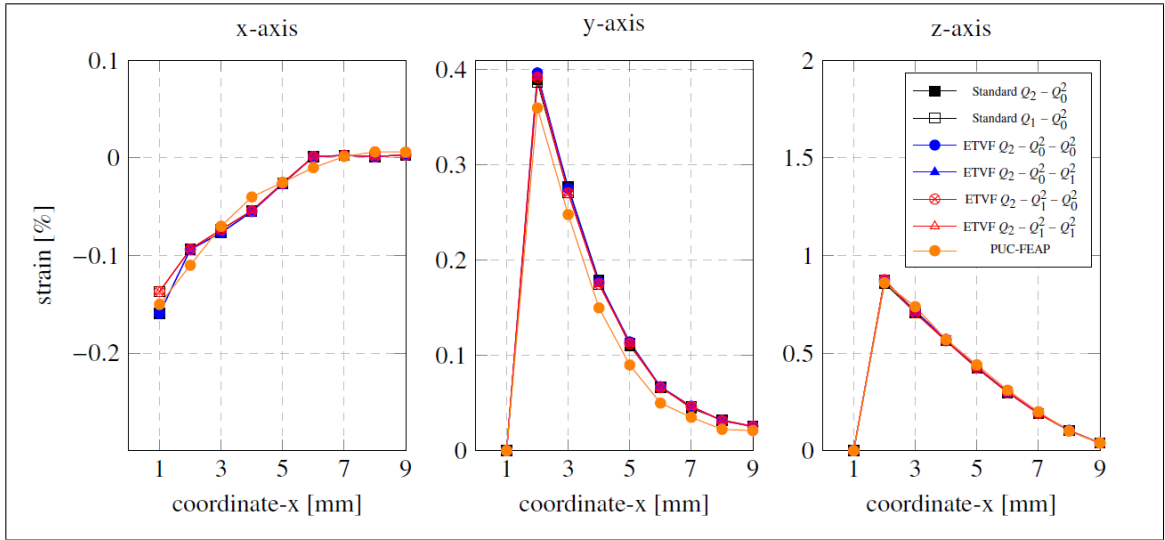


Figure 2.4. Plot of strain along the line in directions of x-, y- and z-axes (quasi-incompressible approach) compared with results obtained by PUC-FEAP team Land et al. (2015).

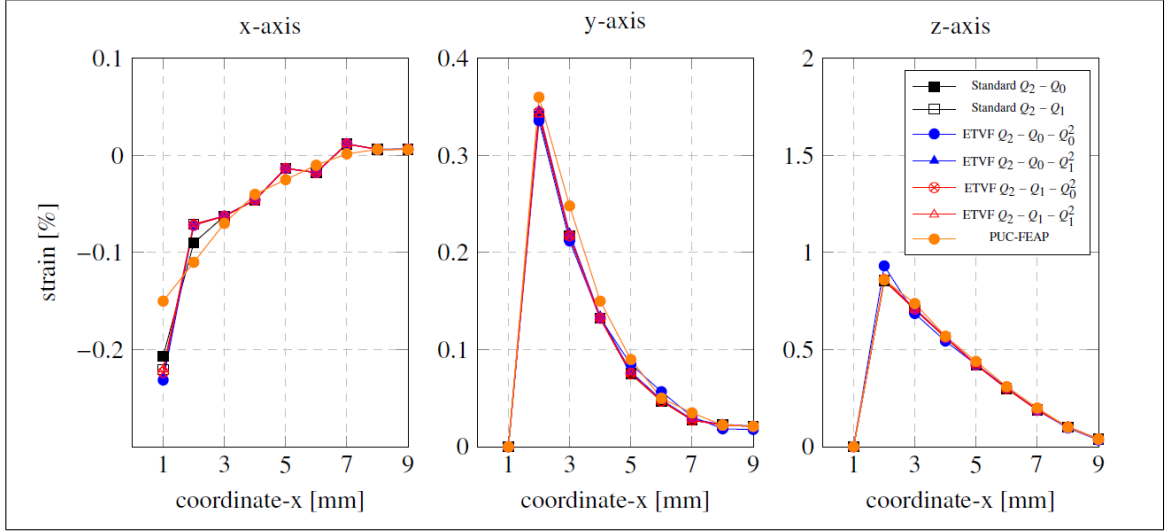


Figure 2.5. Plot of strain along the line in directions of x-, y- and z-axes (full-incompressible approach) compared with results obtained by PUC-FEAP team (Land et al., 2015).

Tables 2.1 and 2.2 report on the numerical performance of the ETVF simulations carried out for the cardiac beam benchmark example in the quasi-incompressible and fully-incompressible cases, respectively. In all cases, the ETVF models resulted in more DOFS than its Standard FE counterpart, reaching a dimension increase of roughly 50% in the quasi-incompressible case using a  $Q_1 - P_0 - Q_1^2$  interpolation scheme. The tip deflection  $\delta_z^{\max}$  corresponds to the vertical displacement experienced by the point (10, 0.5, 1) of the reference configuration. For all interpolation schemes considered, the ETVF model delivered the same tip displacement predicted by the Standard FE model, which are also in close agreement with the tip-displacement values reported in the benchmark study (Land et al., 2015). The  $L^2$  error shows that, in integral terms, the solution of the ETVF problem is very similar to the Standard FE solution. We also note that in all cases, the speed-up values were greater than one, which means that for all interpolation schemes considered the ETVF simulations demanded less wall-clock time than the Standard FE simulations.

Table 2.1. Numerical performance of the ETVF and Standard FE models for the cardiac beam benchmark example in the quasi-incompressible case ( $\kappa = 10^3$ ).

Model				Numerical Performance		
$\varphi$	$\mathbf{p}, \theta$	$\phi, \xi$	ndofs	$\delta_z^{\max}$	$L^2$ error	speed-up
Q2	Q1	-	4,091	4.19	-	-
		Q1	5,819	4.19	3.10E-14	1.62
		P0	4,307	4.19	2.35E-14	1.88
Q1	P0	-	840	4.19	-	-
		Q1	1,256	4.19	1.64E-15	1.47
		P0	1,056	4.19	1.30E-15	1.49

Table 2.2. Numerical performance of the ETVF and Standard FE models for the cardiac beam benchmark example in the fully-incompressible case.

Model				Numerical Performance		
$\varphi$	$\mathbf{p}$	$\phi, \xi$	ndofs	$\delta_z^{\max}$	$L^2$ error	speed-up
Q2	Q1	-	3,883	4.17	-	-
		Q1	4,299	4.17	2.44E-15	1.49
		P0	4,099	4.17	1.98E-13	1.68
	P0	-	3,783	4.20	-	-
		Q1	4,199	4.20	3.76E-13	1.47
		P0	3,999	4.20	1.52E-13	1.50

To study the well-posedness and numerical stability in the solution of the linear systems that arise in each simulation and relate it with the performance of the solver employed, we computed the condition number resulting from the Standard FE and the ETVF methods for different mesh sizes, see Figure 2.6. In general, we observe that the condition number grows with the number of elements in all cases, as expected (Trefethen & Bau, 1997). We note, however, that the condition number in ETVF models is always smaller than that of the Standard FE models for every mesh size analyzed.

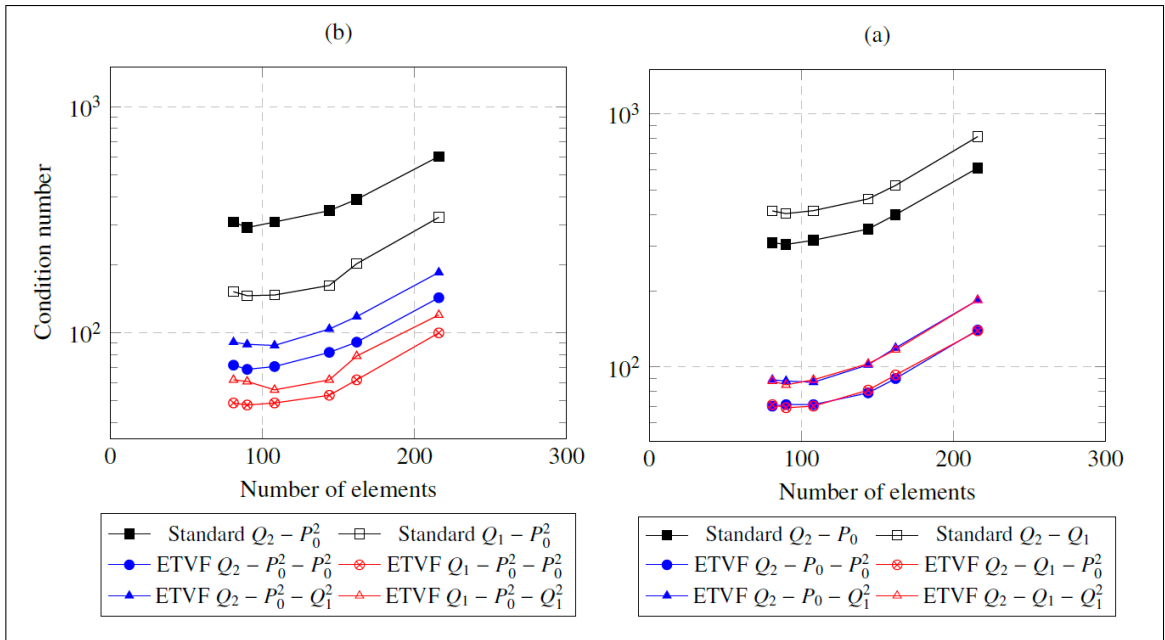


Figure 2.6. Condition number for the cardiac beam benchmark example under different formulations and element interpolation schemes: (a) Quasi-incompressible case (b) Fully-incompressible case

### 2.3.2. Artery inflation

The second example considered in this study is the simulation of the passive mechanical response of a cylindrical artery during inflation, following a study previously reported

in the literature (Holzapfel et al., 2000). Figure 2.1(b) shows the geometry and loading conditions for this example. The loading protocol seeks to simulate the deformation occurring in healthy young arterial segment under pressure levels that vary from 0 to 21.33 kPa, along with an axial extension between 50% and 90%. We discretized the domain using tetrahedral elements, and considered simulations with and without residual stresses. Information about the geometry and the fiber orientation assumed in simulations can be found in Table 2.3. In all simulations we considered the strain energy density function defined in 2.2.2.2, which assumes a two-layer fiber-reinforced composite model for arterial tissue with collagen fibers embedded into a non-collagenous matrix. Figure 2.7(a) shows the distribution of the fiber stretch ( $I_4$ ) on the reference configuration, and Figure 2.7(b) displays the fiber stress distribution on the deformed configuration of the artery.

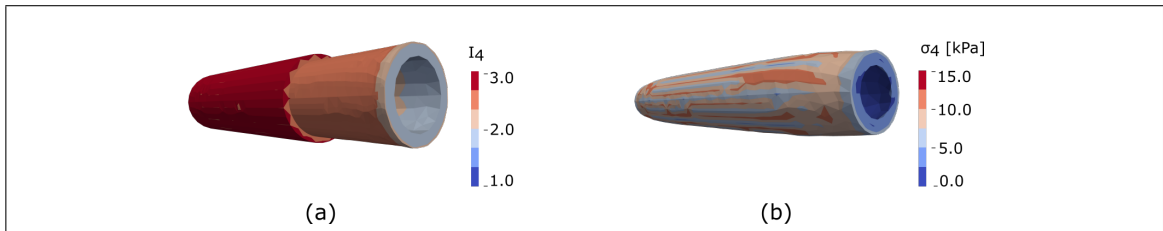


Figure 2.7. Artery inflation simulation. (a) fiber stretch, (b) stress along the fiber direction

Table 2.3. Geometry and fiber orientation for the artery inflation example.

Case	Inner radius $r_i$ [mm]	Outer radius $r_e$ [mm]	Length $L$ [mm]	$\alpha$
with residual stress	1.43	1.82	100	$160^\circ$
without residual stress	0.71	1.10	100	$0^\circ$

The relation between the applied internal pressure versus the internal radius under two levels of axial stretch obtained from ETVF simulations for the cases with and without residual stress is reported in Figure 2.8. Values from the original study are also included to allow for a visual comparison. The ETVF simulations resulted in S-shaped curves that are in very good agreement with the values informed in the literature.

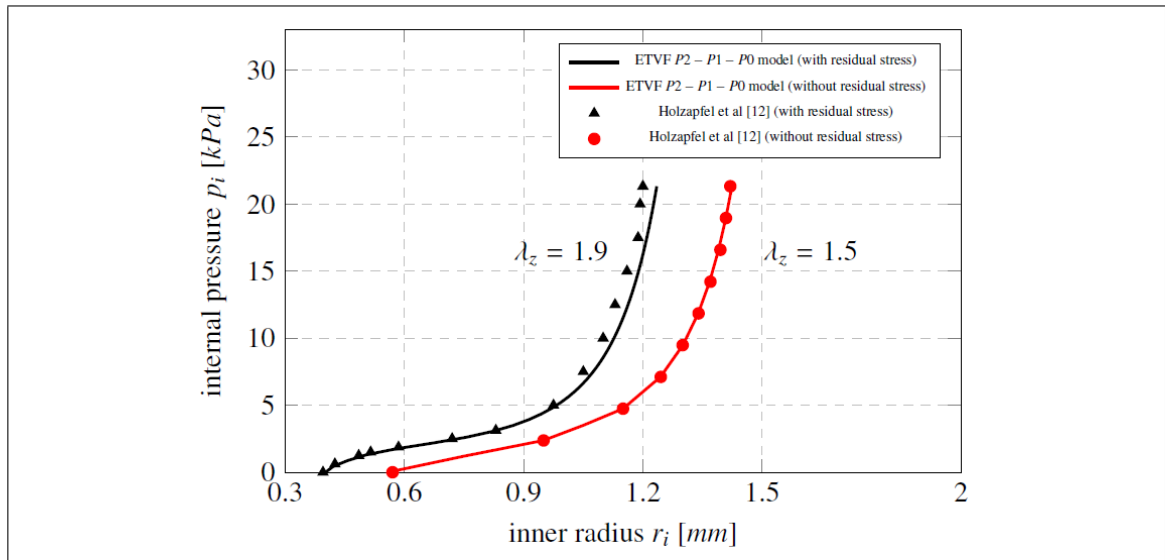


Figure 2.8. Deformation behavior of a carotid artery during inflation and stretching compared with results presented in (Holzapfel et al., 2000).

The numerical performance of the ETVF method using different element interpolation schemes is reported in Tables 2.4 and 2.5 for the quasi- and fully-incompressible approaches, respectively. As expected, the number of DOFs in the ETVF models are always greater than those found for the Standard FE model. The particular case of the ETVF model with a  $P_1 - P_0 - P_0^2$  interpolation scheme results in a dimension increase of 66%. For every interpolation scheme considered, the inner radius in the deformed configuration predicted by the ETVF was virtually the same as that resulting from the Standard FE

model. In addition, we report the relative value of the largest load substep that converges during the first step of the simulation ( $1_p^{st}$ ). We note that the ETVF models deliver a first convergent substep that can be up to  $2.5\times$  that allowed by Standard FE models. The  $L^2$  errors further show that the ETVF solution is very accurate in integral terms when compared to the Standard FE counterpart. In terms of speed-ups, we observe that the ETVF models always deliver values greater than one. The best performance is obtained by the ETVF model using a  $P_1 - P_0 - P_0^2$  element scheme, which delivers a speed-up of 2.18 for the quasi-incompressible case.

Table 2.4. Numerical performance of the ETVF and Standard FE models for the artery inflation example in the quasi-incompressible case ( $\kappa = 10^3$ ).

Model				Numerical Performance			
$\varphi$	$\mathbf{p}$	$\phi, \xi$	ndofs	$r_i$	$1_p^{st}[\%]$	$L^2$ error	speed-up
P2	P1	-	32,959	1.21	6.6	-	-
		P1	36,281	1.21	10.0	7.92E-10	1.50
		P0	42,751	1.21	10.0	7.89E-10	1.52
P1	P0	-	14,775	1.18	4.0	-	-
		P1	18,097	1.18	10.0	3.49E-9	1.71
		P0	24,567	1.18	10.0	1.22E-9	2.18

Table 2.5. Numerical performance of the ETVF and Standard FE models for the artery inflation example in the fully-incompressible case.

Model				Numerical Performance			
$\varphi$	$\mathbf{p}$	$\phi, \xi$	ndofs	$r_i$	$1_p^{st}[\%]$	$L^2$ error	speed-up
P2	P1	-	31,298	1.22	4.0	-	-
		P1	34,620	1.22	5.9	8.10E-12	1.57
		P0	41,090	1.22	5.9	4.12E-12	1.61
	P0	-	34,533	1.21	4.0	-	-
		P1	37,855	1.21	5.9	5.40E-10	1.57
		P0	44,325	1.21	5.9	2.17E-10	1.58

Figure 2.9 shows the condition number in the tangent operators as a function of the number of elements for the artery inflation example. Similarly to the previous example, the condition number increases with the number of elements in all cases considered. Once again, for a fixed number of elements, the ETVF models result in condition numbers that are always smaller than the Standard FE models, reaching in some cases a reduction of roughly one order of magnitude.

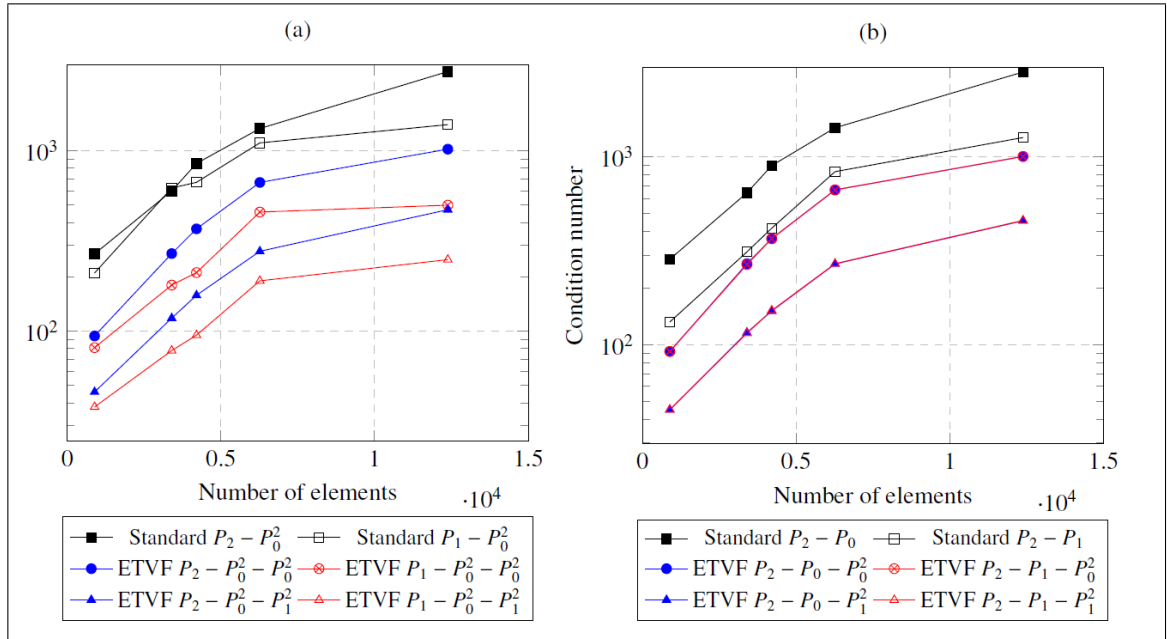


Figure 2.9. Condition number for several discretizations and element combinations for artery inflation. (a) quasi-incompressible case. (b) full-incompressible case.

### 2.3.3. Passive filling of biventricular chambers

As a third example of application, we simulated the mechanical behavior of the heart ventricles during passive filling, see Figure 2.1(c). An end-diastolic pressure of 1.59 kPa (12 mm Hg) was applied on the inner surface of the left ventricle. The right ventricle was loaded on the inner surface with a pressure of 0.32 kPa (2.4 mm Hg). The biventricular domain was obtained from magnetic resonance images of the heart in a human volunteer (Hurtado & Henao, 2014), with an unloaded left-ventricular volume of 39.86 ml. The domain was discretized using 37,127 tetrahedral elements and 8,612 nodes. The top face of the biventricular mesh was clamped and the outer surfaces were assumed to be traction free. Using a rule-based approach (Bayer et al., 2012), the fiber orientation at every point

of our biventricular geometry was computed (Hurtado et al., 2016), see Figure 2.10(a). For the constitutive relation, we considered the structurally-based model for passive myocardium described in 2.2.2.3. Table 2.2 reports the parameter values employed in our simulations, which were taken from the literature (Gao et al., 2017).

Figures 2.10(b), 2.10(c) and 2.10(c) show the distribution in the biventricular domain of the fiber stretch, fiber stress and the von Mises stress, respectively, obtained from the ETVF simulation. High values of fiber stretch and stress are found in the inner surface of the left ventricle. The highest values of von Mises stress were observed in the thinnest region of the outer wall in the right ventricle.

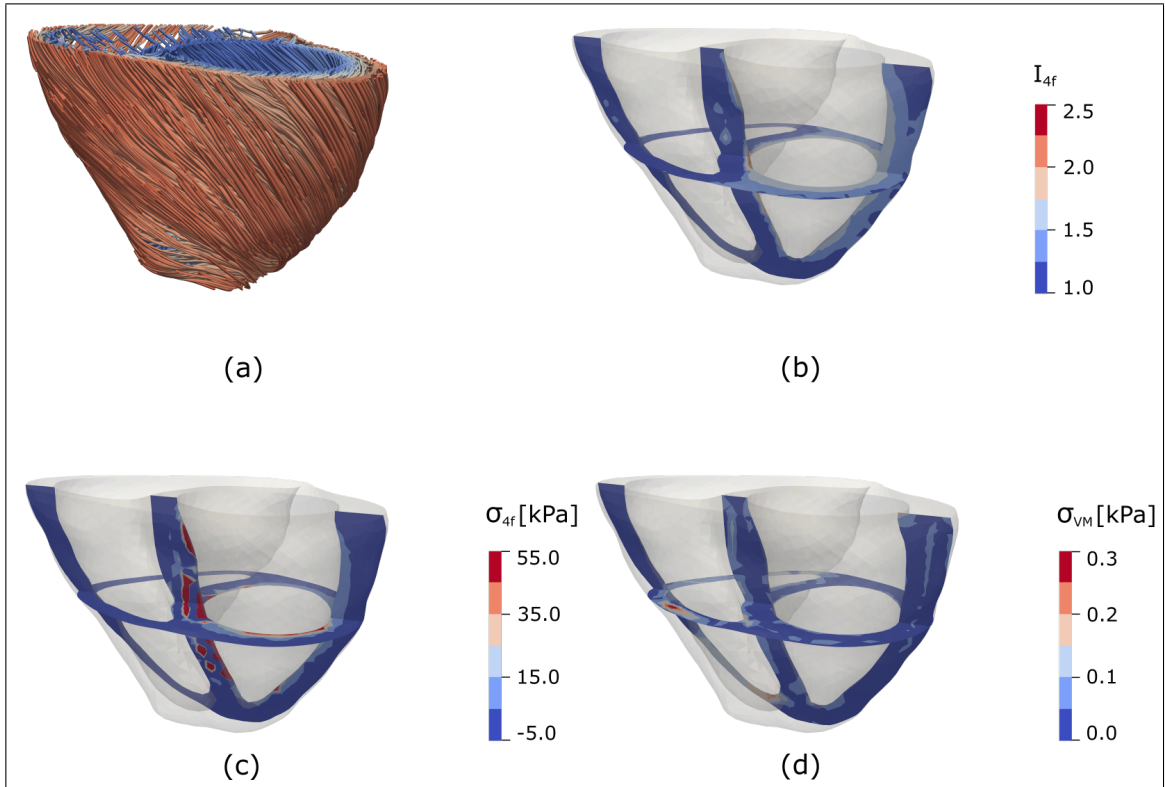


Figure 2.10. (a) : model with fibers included (b): square stretching in the direction of the fiber (c): stress in the direction of the fiber (d): Von Mises stress for the final state.

The numerical performance of the ETVF using different element interpolation schemes and its comparison against the Standard FE model is reported in Tables 2.6 and 2.7 for the quasi- and fully-incompressible approaches, respectively. All ETVF models resulted in a higher number of DOFs when compared to their Standard counterparts, with a maximum dimension increase of 74% for the ETVF model using a  $P_1 - P_0 - P_0^2$  interpolation scheme in the quasi-incompressible case. In all simulations, we computed the left-ventricle end-diastolic volume (EDV), which corresponds to the left-ventricular

cavity volume in the deformed configuration. For the quasi-incompressible and the fully-incompressible cases independently, the EDV predicted by the ETVF and Standard FE models was virtually the same. A similar trend was obtained for the ejection fraction (EF), defined as  $(EDV - ESV)/ESV$ , where the end-systolic volume  $ESV$  is the volume in the left-ventricle cavity in the undeformed configuration. We report the relative value of the largest load substep that converges during the first step of the simulation ( $1_p^{st}$ ). We note that the ETVF models deliver a first convergent substep that can be up to  $1.5 \times$  larger than allowed by Standard FE models. The  $L^2$  error made by the ETVF models was below  $1.0E-9$  and  $1.0E-10$  in the quasi-incompressible and fully-incompressible cases, respectively. In terms of comparing computing time, the interpolation scheme  $P_1 - P_0 - P_1^2$  delivered the highest speed-up of all cases, reaching  $2.28 \times$ , followed by the  $P_1 - P_0 - P_0^2$  scheme that resulted in a speed-up of roughly  $2 \times$ . The condition number of the first step tangent operator was also computed in all simulations, where we observe that the ETVF models delivered condition numbers that were strictly lower than those found in standard FE models. For the quasi-incompressible case, the ETVF model with interpolation scheme  $P_1 - P_0 - P_1^2$  reached a reduction in the condition number of roughly 52% when compared to its Standard FE counterpart.

Table 2.6. Numerical performance of the ETVF and Standard FE models for the biventricular passive inflation example in the quasi-incompressible case ( $\kappa = 10^4$ ).

Model				Volume		Numerical Performance			
$\varphi$	$\mathbf{p}, \theta$	$\phi, \xi$	ndofs	EDV[ml]	EF[%]	$1_p^{st}$ [%]	$L^2$ error	speed-up	condition number
P1	P0	-	100,090	98.02	59.3	3.13	-	-	2.87
		P1	117,314	98.02	59.3	4.68	2.03E-9	2.28	1.37
		P0	174,344	98.02	59.3	4.68	1.02E-9	1.93	1.43

Table 2.7. Numerical performance of the ETVF and Standard FE models for the biventricular passive inflation example in the fully-incompressible case.

Model				Volume		Numerical Performance			
$\varphi$	p	$\phi, \xi$	ndofs	EDV[ml]	EF[%]	$1_p^{\text{st}}$ [%]	$L^2$ error	speed-up	condition number
P2	P1	-	185,990	94.20	57.7	3.33	-	-	4.22
		P1	203,214	94.20	57.7	4.35	1.40E-12	1.63	2.83
		P0	231,729	94.20	57.7	4.35	8.90E-10	1.57	2.82
	P0	-	214,505	94.20	57.7	3.33	-	-	4.30
		P1	260,244	94.20	57.7	4.76	3.38E-11	1.62	2.83
		P0	288,759	94.20	57.7	4.76	9.90E-12	1.67	2.82

## 2.4. Discussion

In this work, we have introduced a novel energy-transform variational formulation to solve finite-elasticity problems in cardiac and vessel mechanics. To this end, auxiliary fields are introduced in the formulation using the method of Lagrange multipliers, both considering the quasi-incompressible as well as the fully-incompressible regimes. The novelty of our work relies on conveniently transforming the energy into a quadratic form using auxiliary variables, whose constraints are transformed using simple functions that can reduce the non-linearity of the functional in the variational formulation. Further, a multi-field Galerkin finite-element scheme is introduced to numerically solve the proposed formulation, which is demonstrated both in a simplified and realistic vessel and cardiac biomechanics problems.

As a first validation of our computational framework, we considered the benchmark problems of a cardiac beam proposed by Land and collaborators (Land et al., 2015), and

the inflation of an artery model developed by Holzapfel, Gasser and Ogden (Holzapfel et al., 2000). We solved these problems by reformulating them into the framework of ETVF and employed four different element interpolation schemes in their numerical solution. We considered the solution to these problems as a baseline using standard FE methods widely employed in the literature, i.e., displacement-pressure (u-p) mixed FE schemes for the incompressible cases and three-field Hu-Washizu variational formulations for the quasi-incompressible cases. Figure 2.4 shows the predictions of the ETVF against the standard FE methods and the reported strain curves from the literature for the cardiac beam example. In general, the outcomes from the ETVF closely follows the benchmark study for all cases of interpolation schemes. A similar result is obtained for the fully-incompressible case, see Figure 2.5, where virtually no differences arise between all methods analyzed. When assessing the performance of the ETVF against the solution of traditional FE discretizations, both for the quasi-incompressible and fully-incompressible cases, we observe that the tip displacement of the cardiac bar is similar in all cases and that the global error measured in terms of the  $L^2$  norm is always below  $10^{-12}$ , indicating that all discretizations of the ETVF converge to the solution provided by standard FE methods, see Tables 2.1 and 2.2. For the problem of the inflation of an artery, similar results are obtained. Figure 2.8 displays how the ETVF method delivers curves of inner radius vs. internal pressure that closely follows the results reported in the literature with and without considering residual stresses (Holzapfel et al., 2000). The internal radius  $r_i$  at the end of the simulation is presented in Table 2.4 and Table 2.5 for the case of quasi-incompressible and incompressible materials, respectively. We found virtually no differences between the standard FE methods and the proposed ETVF schemes. Further, from a global point of view, the  $L^2$  error between ETVF and standard methods in both cases is always below  $3.49 \times 10^{-9}$ . These results show that the ETVF delivers a numerical solution that resembles those predicted by traditional FE schemes. To demonstrate the applicability of the ETVF in anatomically- and structurally-detailed problems, we solved the passive inflation of a human biventricular domain whose geometry was obtained from

patient-specific magnetic-resonance images, and the fiber orientation was constructed using rule-based algorithms (Hurtado et al., 2016). The end-diastolic volume (EDV) and ejection fraction (EF) obtained from simulations based on the ETVF do not differ from the results found from traditional FE simulations, see Tables 2.6 and 2.7. Further, the EF values found in our simulations are in the order of those reported in the literature using a similar patient-specific quasi-incompressible model that reaches an EF of 51% (Gao et al., 2017).

From the numerical performance perspective, we have demonstrated that ETVF models can effectively reduce the computing time of vessel and cardiac biomechanics simulations. In effect, we reached important speed-ups in all of the problems analyzed in this work, which were always higher than 1, indicating that the ETVF method resulted in a reduction of the computing time when compared to standard FE schemes. For the case of the cardiac beam, the most significant speed-up obtained was 1.88 using an ETVF with a  $P_2 - P_1 - P_0^2$  element formulation. This speed-up translates in a reduction of up to 46% of the computing time for this particular simulation. Similarly, for the artery inflation simulation, a speed-up of 2.18 is obtained when using a  $P_1 - P_0^2 - P_0^2$  element formulation, which represents a saving in computing time of roughly 55%. Interestingly, the highest speed-ups were obtained for the simulation of the patient-specific biventricular passive filing problem, where the ETVF with a  $P_1 - P_0^2 - P_1^2$  element formulation achieved a speed-up of 2.28, which reduces the computing time to a third of the time a traditional FE scheme needs. More interestingly, the case of the quasi-incompressible ETVF model using a  $P_1 - P_0 - P_0^2$  interpolation scheme resulted in a problem-dimension increase of 75%, yet the computing time was reduced to practically by 50%. These results are remarkable, especially considering the high spatial heterogeneity and marked structural anisotropy that a cardiac model of the human heart imposes.

To explain why the ETVF method successfully reduced the computing time of complex computational problems, we studied the condition number of all the simulations included in this work. We recall that large-scale systems resulting from the linearization of non-linear problems in the finite-element analysis are typically solved using Krylov-subspace iterative methods such as the Generalized Minimal Residual (GMRES) method (Saad & Schultz, 1986). The convergence of the GMRES method is governed by the following upper bound, developed in the literature (Trefethen & Bau, 1997).

$$\frac{\|\mathbf{r}_n\|}{\|\mathbf{b}_n\|} \leq \kappa(\mathbf{V}) \inf_{p_n \in \mathcal{P}_n} \|p_n\|_{\Lambda(\mathbf{A})}. \quad (2.114)$$

In (2.114),  $\Lambda(\mathbf{A})$  is the set of eigenvalues of  $\mathbf{A}$ ,  $\mathbf{V}(\mathbf{A})$  is a non-singular matrix of eigenvectors of  $\mathbf{A}$ ,  $\mathbf{r}_n$  is the residual at the step  $n$  (i.e  $\mathbf{r}_n = \mathbf{A}\mathbf{x}_n$ ),  $\mathbf{b}_n$  is right side in the linear system in the step  $n$ ,  $p_n$  is the characteristic polynomial of order  $\leq n$ , and  $\kappa(\mathbf{V})$  is the condition number of  $\mathbf{V}$ . Since a reduction of the condition number directly implies a reduction in the number of iterations needed to convergence, see bound (2.114), we conclude that the ETVF achieves important speed-ups in computing time by drastically reducing the condition number, see Table 2.6 and Table 2.7. We remark that the reduction in the condition number is obtained independently of the compressibility approach assumed for the material, and is consistent across all the examples analyzed in this work, where for the same problem a smaller condition number is obtained when using the ETVF formulation instead of the traditional FE formulation, regardless of the discretization scheme. Further, we note that while a finer discretization does increase the condition number in all of the ETVF schemes, it scales with a factor in logarithmic scale that is similar to that obtained using traditional FE schemes, thus keeping the condition number always smaller than that of the standard FE simulation, see Figure 2.6 and Figure 2.9.

We conclude that the ETVF is effective in delivering accurate biomechanical simulations of vessels and the heart at the same time that it considerably improves the computational efficiency in terms of wall-clock time. This acceleration in numerical performance is achieved by reducing the condition number of the system of equations associated with the simulation under analysis, and proved to be effective both in quasi-incompressible and fully-incompressible cases. One limitation of the method is the increase in the number of degrees of freedom needed to formulate an ETVF scheme, which can translate into a considerable increase in the dimension of the linear systems to be solved. Consequently, the implementation of simulations based in the ETVF represents a higher demand for computer memory. Future developments should evaluate the use of enhanced element interpolation schemes that have shown to improve the numerical efficiency of cardiac simulations without impacting their accuracy (Jilberto & Hurtado, 2018). Despite this potential limitation, we note that reducing the condition number of the system has a higher effect than the increase of the dimensionality of the linear system to be solved, as simulations based on the ETVF always results in notable reductions in the computing times, as demonstrated throughout in this work. These results can be auspicious when considering the scalability of the method to large-scale problems with millions of degrees of freedom, making this method very attractive to parallel implementations.

### 3. CONCLUSION

In this thesis, we introduced a novel energy-transformed variational formulation (ETVF) for the hyperelastic problem in soft-tissue mechanics. We tested the performance of ETVF through numerical simulations, including cardiac and artery models composed of several hyperelastic materials. Then, we compared the results obtained by ETVF implementations against the delivered by Standard models. Additionally, we measured the computing time to analyze the linear iterative solver's performance for both methods in each simulation. We demonstrated that ETVF accelerates the resolution of the hyperelastic problem for biomechanical simulations without losing accuracy. In particular, we found that a significant reduction in the condition number of the system is achieved using the ETVF framework instead of traditional implementations, which translates into accelerations in the linear iterative solver (GMRES).

Although ETFV notably accelerates the simulations, we observed that this framework increases the demand for computer memory by introducing new mixed fields, which increasing the dimensionality of the linear system of equations. However, we discovered that reducing the condition number has a more significant effect in the linear solver's performance than increasing the dimensionality of the system. The ETVF framework can be promising for future implementations, including HPC into large-scale and customized problems, and combined with other numerical techniques that had shown to increase the numerical efficiency of biomechanical simulations without impacting their accuracy.

## 4. FUTURE WORK

The work presented in this thesis opens the door to several opportunities for the computational medicine community. As we have demonstrated in Section 2.3, the ETVF framework can drastically accelerate biomechanical simulations without losing accuracy. However, future work can be oriented to improve even further this framework and combining it with other techniques to achieve even better results. For example, despite the speed-ups delivered by the ETVF implementation against Standard FE formulations, ETVF formulations notably increase the system's degrees of freedom. The latter could be reduced with numerical techniques in the mean dilatation procedure to solve the ETVF equations locally (Bonet & Wood, 2008) or with enhanced element interpolation schemes that have been shown to improve the numerical efficiency of cardiac simulations without impacting their accuracy (Jilberto & Hurtado, 2018). Further work could aim to implement the ETVF framework and use advanced preconditioners to improve the iterative performance of the solver in the solution of the linear system that arises in each Newton iteration into these non-linear FE problems (Campos et al., 2018).

Another promising possibility is to combine the ETVF framework with high-performance computing (HPC). The ETVF framework can be implemented into very detailed and customized models, with several millions of DOF's, and take advantage of the parallelization of non-linear FE codes to reduce the computing time for these types of simulations (Lafortune et al., 2012; Augustin et al., 2014). Moreover, this methodology could be applied to reproduce the active behavior of soft tissues and compare its performance against Standard formulations for these cases. Applying the ETVF framework could improve the solver's performance into non-linear FE problems, such as the active contraction of the cardiac muscle, and could broaden the spectrum and impact of this investigation and any subsequent work. Finally, since the ETVF formulation notably increases DOFs of the system, and these types of simulations are computationally very challenging, we think it

is crucial to implement the mean dilation procedure to solve the new ETVF mixed fields before all the others alternatives.

## BIBLIOGRAPHY

Augustin, C. M., Holzapfel, G. A., & Steinbach, O. (2014). Classical and all-floating FETI methods for the simulation of arterial tissues. *International Journal for Numerical Methods in Engineering*, 99(4), 290–312.

Bayer, J. D., Blake, R. C., Plank, G., & Trayanova, N. A. (2012). A novel rule-based algorithm for assigning myocardial fiber orientation to computational heart models. *Annals of Biomedical Engineering*, 40(10), 2243–2254.

Bonet, J., & Wood, R. (2008). *J. bonet, r. d. wood, nonlinear continuum mechanics for finite element analysis, cambridge university press, cambridge, uk* (Vol. 24). doi: 10.1017/CBO9780511755446

Campos, J. O., dos Santos, R. W., Sundnes, J., & Rocha, B. M. (2018). Preconditioned augmented lagrangian formulation for nearly incompressible cardiac mechanics. *International Journal for Numerical Methods in Biomedical Engineering*, 34(4), e2948.

Chagnon, G., Rebouah, M., & Favier, D. (2015). Hyperelastic Energy Densities for Soft Biological Tissues: A Review. *Journal of Elasticity*, 120(2), 129–160.

Chuong, C. J., & Fung, Y. C. (1983). Three-dimensional stress distribution in arteries. *Journal of Biomechanical Engineering*, 105(3), 268–274.

Delfino, A., Stergiopoulos, N., Moore, J., & Meister, J.-J. (1997). Residual strain effects on the stress field in a thick wall finite element model of the human carotid bifurcation. *Journal of Biomechanics*, 30(8), 777 - 786.

Fung, Y. C. (1993). *Biomechanics. mechanical properties of living tissues*. Springer-Verlag New York.

- Gao, H., Feng, L., Qi, N., Berry, C., Griffith, B. E., & Luo, X. (2017). A coupled mitral valve—left ventricle model with fluid–structure interaction. *Medical Engineering & Physics*, *47*, 128 - 136.
- García-Herrera, C. M., & Celentano, D. J. (2013). Modelling and numerical simulation of the human aortic arch under in vivo conditions. *Biomechanics and modeling in mechanobiology*, *12*(6), 1143–1154.
- Gasser, O. R. W. . H. G. A., T. C. (2006). Hyperelastic modelling of arterial layers with distributed collagen fibre orientations. *Journal of the Royal Society, Interface*, *3*((6)), 15–35.
- Gasser, T., Auer, M., Labruto, F., Swedenborg, J., & Roy, J. (2010). Biomechanical rupture risk assessment of abdominal aortic aneurysms: Model complexity versus predictability of finite element simulations. *European Journal of Vascular and Endovascular Surgery*, *40*(2), 176 - 185.
- Göktepe, S., Acharya, S., Wong, J., & Kuhl, E. (2011). Computational modeling of passive myocardium. *International Journal for Numerical Methods in Biomedical Engineering*, *27*, 1–12.
- Guccione, J. M., McCulloch, A. D., & Waldman, L. K. (1991). Passive material properties of intact ventricular myocardium determined from a cylindrical model. *Journal of biomechanical engineering*, *113*(February), 42–55.
- Guyton, A. C., & Hall, J. E. (2016). *Textbook of medical physiology*. Elsevier.
- Hadjicharalambous, M., Lee, J., Smith, N. P., & Nordsletten, D. A. (2014). A displacement-based finite element formulation for incompressible and nearly-incompressible cardiac mechanics. *Computer Methods in Applied Mechanics and Engineering*, *274*, 213–236.

Holzapfel, G. A., Gasser, T. C., & Ogden, R. W. (2000). A new constitutive framework for arterial wall mechanics and a comparative study of material models. *Journal of Elasticity*, 61(1-3), 1–48.

Holzapfel, G. A., & Ogden, R. W. (2009). Constitutive modelling of passive myocardium: a structurally based framework for material characterization. *Philosophical transactions. Series A, Mathematical, physical, and engineering sciences*, 367(1902), 3445–75.

Humphrey, J. (1995). Mechanics of the arterial wall: review and directions. *Critical reviews in biomedical engineering*, 23(1-2), 1—162.

Humphrey, J. D. (2002). *Cardiovascular solid mechanics: cells, tissues, and organs* (Vol. 1). Springer-Verlag New York.

Hunter, P. J., & Smaill, B. H. (1988). The analysis of cardiac function: A continuum approach. *Progress in Biophysics and Molecular Biology*, 52(2), 101–164.

Hurtado, D. E., Castro, S., & Gizzi, A. (2016). Computational modeling of non-linear diffusion in cardiac electrophysiology: A novel porous-medium approach. *Computer Methods in Applied Mechanics and Engineering*, 300, 70 - 83.

Hurtado, D. E., & Henao, D. (2014). Gradient flows and variational principles for cardiac electrophysiology: Toward efficient and robust numerical simulations of the electrical activity of the heart. *Computer Methods in Applied Mechanics and Engineering*, 273, 238 - 254.

Hurtado, D. E., & Rojas, G. (2018). Non-conforming finite-element formulation for cardiac electrophysiology: an effective approach to reduce the computation time of heart simulations without compromising accuracy. *Computational Mechanics*, 61(4), 485–497.

Iaizzo, P. A. (2015). *Handbook of cardiac anatomy, physiology, and devices*. Springer,

Cham.

Jilberto, J., & Hurtado, D. E. (2018). Semi-implicit non-conforming finite-element schemes for cardiac electrophysiology: A framework for mesh-coarsening heart simulations. *Frontiers in Physiology*, *9*, 1513.

Lafortune, P., Arís, R., Vázquez, M., & Houzeaux, G. (2012). Coupled electromechanical model of the heart: Parallel finite element formulation. *International Journal for Numerical Methods in Biomedical Engineering*, *28*(1), 72-86.

Land, S., Gurev, V., Arens, S., Augustin, C. M., Baron, L., Blake, R., ... Niederer, S. A. (2015). Verification of cardiac mechanics software: benchmark problems and solutions for testing active and passive material behaviour. *Proceedings. Mathematical, physical, and engineering sciences / the Royal Society*, *471*(2184), 20150641.

LeGrice, I. J., Smaill, B. H., Chai, L. Z., Edgar, S. G., Gavin, J. B., & Hunter, P. J. (1995). Laminar structure of the heart: ventricular myocyte arrangement and connective tissue architecture in the dog. *American Journal of Physiology-Heart and Circulatory Physiology*, *269*(2), H571-H582.

Logg, A., Mardal, K.-A., Wells, G. N., et al. (2012). *Automated solution of differential equations by the finite element method* (A. Logg, K.-A. Mardal, & G. N. Wells, Eds.). Springer.

MacCallum, J. B. (1900). On the muscular architecture and growth of the ventricles of the heart. *Welch Festschrift*, *9*, 307–335.

Malkus, D. S., & Hughes, T. J. R. (1978). Mixed finite element methods - Reduced and selective integration techniques: A unification of concepts. *Computer Methods in Applied Mechanics and Engineering*, *15*(1), 63–81.

- Mei, Y., Hurtado, D. E., Pant, S., & Aggarwal, A. (2018). On improving the numerical convergence of highly nonlinear elasticity problems. *Computer Methods in Applied Mechanics and Engineering*, 337, 110–127.
- Nash, M. P., & Hunter, P. J. (2001). Computational mechanics of the heart. *Journal of Elasticity*, 61, 113–141.
- Nordsletten, D., Niederer, S., Nash, M., Hunter, P., & Smith, N. (2011). Coupling multiphysics models to cardiac mechanics. *Progress in Biophysics and Molecular Biology*, 104(1), 77 - 88.
- Ogden, R. (1997). *Non-linear elastic deformations*. Dover Publications.
- Pezzuto, S., Hake, J., & Sundnes, J. (2016). Space-discretization error analysis and stabilization schemes for conduction velocity in cardiac electrophysiology. *International Journal for Numerical Methods in Biomedical Engineering*.
- Quarteroni, A., Lassila, T., Rossi, S., & Ruiz-Baier, R. (2017). Integrated Heart—Coupling multiscale and multiphysics models for the simulation of the cardiac function. *Computer Methods in Applied Mechanics and Engineering*, 314, 345–407.
- Saad, Y., & Schultz, M. H. (1986). Gmres: A generalized minimal residual algorithm for solving nonsymmetric linear systems. *SIAM Journal on Scientific and Statistical Computing*, 7(3), 856-869.
- Simo, J. C., Taylor, R. L., & Pister, K. S. (1985). Variational and projection methods for the volume constraint in finite deformation elasto-plasticity. *Computer Methods in Applied Mechanics and Engineering*, 51(1-3), 177–208.
- Streeter, D. P. P. J. R., Henry M Spotnitz, & Sonnenblick, E. H. (1969). Fiber orientation in the canine left ventricle during diastole and systole. , 24(3), 339—347.

Sundnes, J., Wall, S., Osnes, H., Thorvaldsen, T., & McCulloch, A. D. (2012). Improved discretisation and linearisation of active tension in strongly coupled cardiac electro-mechanics simulations. *Computer Methods in Biomechanics and Biomedical Engineering*, *17*(6), 604–615.

Trefethen, L. N., & Bau, D. (1997). *Numerical linear algebra*. SIAM.

Vigueras, G., Roy, I., Cookson, A., Lee, J., Smith, N., & Nordsletten, D. (2014). Toward GPGPU accelerated human electromechanical cardiac simulations. *International Journal for Numerical Methods in Biomedical Engineering*, *30*(1), 117–134.

Vossoughi, J. (1993). Ii. intimal residual stress and strain in large arteries. *1993 Bioengng. Conf.*

Wall, S. T., Walker, J. C., Healy, K. E., Ratcliffe, M. B., & Guccione, J. M. (2006). Theoretical impact of the injection of material into the myocardium: A finite element model simulation. *Circulation*, *114*(24), 2627–2635.

Winslow, R. L., Trayanova, N., Geman, D., & Miller, M. I. (2012). Computational medicine: Translating models to clinical care. *Science Translational Medicine*, *4*(158), 158rv11–158rv11.